

Wavefield Characterisation of MHz XFEL Pulses

Author:

Trey Wilson GUEST

Supervisors:

Prof. Brian ABBEY

Dr Grant VAN RIESSEN

A thesis submitted in fulfillment
of the requirements for the degree of
Doctor of Philosophy

Department of Chemistry and Physics
School of Molecular Sciences
College of Science, Health and Engineering



La Trobe University
Victoria, Australia

— —

Wavefield Characterisation of MHz XFEL Pulses, © — -

Author:

Trey Wilson GUEST

Supervisors:

Prof. Brian ABBEY

Dr Grant VAN RIESSEN

Institute:

La Trobe University, Victoria, Australia

CONTENTS

List of Listings	v
List of Algorithms	vi
1 INTRODUCTION	1
2 LITERATURE REVIEW	3
2.1 Properties of X-rays	3
2.1.1 First Principles: Maxwell and Helmholtz Equations	3
2.1.2 Propagation of X-rays in a Free-Space	4
2.1.3 Angular Spectrum Representation	4
2.1.4 Fresnel Diffractor	6
2.1.5 Sampling Requirements of the Fresnel Propagator	7
2.1.6 The Huygens-Fresnel Convolution Propagator	8
2.1.7 Fraunhofer Diffraction	9
2.2 X-ray Imaging	10
2.2.1 Interaction of Light with Matter	10
2.2.2 The Projection Approximation	12
2.2.3 Optical Coherence	14
2.2.4 Partial Coherent Imaging	17
2.3 X-ray Free Electron Lasers	19
3 THE SPB-SFX MODEL	24
3.1 Introduction	24
3.1.1 The SPB-SFX Instrument	25
3.2 Method	26
3.2.1 The Coherent Source Model	26
3.2.2 The Partially Coherent Source Model	34
3.3 Results and Discussion	34
3.3.1 Discussion	35
3.4 Conclusions	35
4 POINTING INSTABILITY AT THE SPB-SFX INSTRUMENT	36
4.0.1	36
4.0.2	36
5 PHASE-RETRIEVAL METHODS FOR MHZ XFELS	37

5.1	Introduction	37
5.2	Virtual Reference Single-Shot Phase-Retrieval	37
5.2.1	Absolute Mode	38
5.2.2	Special Case	40
5.2.3	Differential Mode	40
6	APPENDIX: VECTOR IDENTITIES	41
7	APPENDIX: BEAMLINE PROPERTIES	42
	BIBLIOGRAPHY	44

LIST OF LISTINGS

LIST OF ALGORITHMS

INTRODUCTION

The development of X-ray Free Electron Laser (FEL) facilities has been motivated by the promise of single-particle imaging (SPI) of biomolecules at atomic-scale resolutions [1] as an extension to contemporary macromolecular crystallography (MX) techniques using third-generation synchrotron light sources. While the theoretical resolution limit of hard x-ray FEL SPI experiments ($\approx 3\text{\AA}$) improves upon the diffraction limits of optical ($\approx 200\text{ nm}$) and electron ($\approx 1\text{ nm} - 10\text{ nm}$) microscopies [2], the small scattering cross section of organic materials in the hard x-ray regime [3] necessitates samples to be crystallised to improve diffraction efficiencies [4].

The resolution of structural information obtained via MX using coherent synchrotron radiation is limited by crystal quality and radiation damage. Protein crystallography is a multivariate process and the optimisation of experimental conditions to achieve well-diffracting protein crystals is a field-in-itself [5]. In general, protein structural determination is limited to the case of easily crystallised materials, restricting the scope of the technique. As in Cryogenic Electron Microscopy (Cryo-EM), radiation damage in MX is typically overcome by cryogenic freezing of the sample, which restricts the study of temporal dynamics and has been demonstrated to bias structural information [6].

The use of X-ray Free Electron Lasers (XFELs) light sources in structural biology is predicated on the principle that high-flux X-ray sources provide sufficient scattering signal from amorphous materials to circumvent the need for crystallisation [7]. While it was initially believed that the radiation dose required for high-resolution elastic scattering would lead to inelastic processes that destroy the molecule during imaging, theoretical work [8] suggested that sufficiently short X-ray pulses could outrun the sample damage process. This has since been demonstrated in simulation [9] and experiment [10] and has encouraged the construction of dedicated SPI instruments at LCLS [11] and the European XFEL [12]).

Remediation of strict sample requirements in X-ray protein structure determination enable novel approaches to structural biology. The capacity to image amorphous materials due to the high-brightness of XFEL sources enables the study of previously unavailable classes of molecules, and the reduced dependence on sam-

ple damage mitigation due to ultra-fast pulse times allows the imaging of proteins and biomolecules in their native state. The development of the fast-repetition rate XFEL source at the European XFEL [13] extends these science opportunities by enabling the exploration of temporal sample dynamics at megahertz intervals [14].

Despite early successes in SPI using XFEL sources, experimental resolutions are far-removed from the theoretical minimum [15], [16]. While the optimisation of XFEL imaging shares some technical analogies with conventional imaging techniques (i.e. maximisation of detector efficiency and resolution), the primary inhibitors to atomic resolution are unique to the generation and transport of XFEL sources [1].

The generation of photon-beams by the Self-Amplified Spontaneous Emission (SASE) radiation of relativistic electrons is an inherently stochastic process [17]. While transverse mode selection leads to an effectively spatially coherent source, inhomogenous broadening and energy spread result in spatially incoherent, quasi-stationary random pulses [18], which manifest as pulse-to-pulse instabilities that have been implicated in the degradation of contemporary SPI applications [19]–[23]. Issues regarding source fluctuations are compounded by challenges in optical transport, which impose strict fabrication requirements [24].

To maximise the capabilities of XFEL radiation, the SPI roadmap [25] identifies the development of ‘drop-in’, shot-to-shot wavefield sensing mechanisms at the XFEL focus among the primary milestones in achieving atomic resolution, with the hope of future extension to parasitic, online wavefront characterisation schemes [25]. Direct measurement of XFEL focii are limited by both the insufficient spatial resolution of contemporary detectors and the damage caused. In the absence of suitable wavefront sensing mechanism, we pursue a description of the SPB-SFX instrument focus under different operational conditions by construction of a wave-optics model. To date, no discussion of the properties of individual XFEL pulses at the instrument focus exists.

LITERATURE REVIEW

2.1 PROPERTIES OF X-RAYS

2.1.1 *First Principles: Maxwell and Helmholtz Equations*

We begin our disucssion of X-rays with the free-space Maxwell equations:

$$\nabla \cdot \mathbf{E}(x, y, z, t) = 0 \quad (2.1)$$

$$\nabla \cdot \mathbf{B}(x, y, z, t) = 0 \quad (2.2)$$

$$\nabla \times \mathbf{E}(x, y, z, t) + \frac{\partial}{\partial t} \mathbf{B}(x, y, z, t) = 0 \quad (2.3)$$

$$\nabla \times \mathbf{B}(x, y, z, t) - \epsilon_0 \mu_0 \frac{\partial}{\partial t} \mathbf{E}(x, y, z, t) = 0 \quad (2.4)$$

where \mathbf{E} and \mathbf{B} are the electric field and magnetic induction vectors¹, ϵ_0 and μ_0 are the electrical and magnetic permittivity of free-space, and ∇ and $\nabla \times$ denote the gradient and curl operators of the three-dimensional coordinate system: $x, y, z \in \mathbb{R}$. Using the vector identity [Equation 6.1] and taking the curl of Equation 2.3 we get

$$\nabla [\nabla \cdot \mathbf{E}(x, y, z, t)] - \nabla^2 \mathbf{E}(x, y, z, t) + \nabla \times \frac{\partial}{\partial t} \mathbf{B}(x, y, z, t) = 0 \quad (2.5)$$

$$\Rightarrow \nabla^2 \mathbf{E}(x, y, z, t) = \frac{\partial^2}{\partial t^2} \epsilon_0 \mu_0 \mathbf{E}(x, y, z, t) \quad (2.6)$$

which can be used to obtain the d'Alembert wave equation using the fact that $\epsilon_0 \mu_0 = c^{-2}$:

$$\left(\frac{1}{c^2} \frac{\partial^2}{\partial t^2} - \nabla^2 \right) \mathbf{E}(x, y, z, t) = 0, \quad (2.7)$$

¹ where the bold format, unless stated otherwise, will be used throughout this text to denote vector notation

which can be equivalently obtained for the magnetic induction vector:

$$\left(\frac{1}{c^2} \frac{\partial^2}{\partial t^2} - \nabla^2 \right) \mathbf{B}(x, y, z, t) = 0, \quad (2.8)$$

which illustrates that each of the three spatial components of the free-space electric field and the free-space magnetic induction are uncoupled from each other.

Finally, we note that either of these vector fields can be replaced by a single, complex scalar field function E describing an electromagnetic disturbance in space-time:

$$\left(\frac{1}{c^2} \frac{\partial^2}{\partial t^2} - \nabla^2 \right) E(x, y, z, t) = 0, \quad (2.9)$$

which has the observable optical intensity I :

$$I(x, y, z, t) = |E(x, y, z, t)|^2. \quad (2.10)$$

2.1.2 Propagation of X-rays in a Free-Space

Any electromagnetic field that obeys the d'Alembert equation (Equation 2.9) can be decomposed into a superposition of its monochromatic components via the Fourier transform:

$$E(x, y, z, t) = \frac{1}{\sqrt{2\pi}} \int_0^\infty E_\omega(x, y, z) \exp(-i\omega t) d\omega \quad (2.11)$$

where each E_ω denotes the spatial wavefield² for a single temporal frequency ω . We label the RHS of Equation 2.11 as the monochromatic signal form of the electromagnetic disturbance E . Substituting Equation 2.11 into Equation 2.9 and defining the wavevector $k : k = \frac{\omega}{c}$ we obtain the Helmholtz equation for each of the components of the decomposed polychromatic field:

$$(\nabla^2 + k^2) E_\omega(x, y, z) = 0. \quad (2.12)$$

2.1.3 Angular Spectrum Representation

With an understanding of the spectral decomposition of a wavefield, we move to define an operator which models the evolution of any suitably defined wavefield

² Here we choose to distinguish between a wavefield as an electromagnetic disturbance defined in 3 spatial and 3 phase-space dimensions, as opposed to a wavefront, which we define to be a surface of constant phase. We restrict any use of the term wavefunction to describe probabilistic fields.

in an arbitrary parallel plane, i. e. we pursue $E(x, y, z = \Delta z)$ from $E(x, y, z = 0)$.

Construct a Cartesian coordinate system with a monochromatic plane-wave defined in the plane of origin at $z = 0$. Maintain that the wave is forward propagating: there is no points in the plane of origin where the flow of optical energy is right-to-left. Let E_ω be the component of the monochromatic signal corresponding to the mean spectral frequency component of E and consider the wave-vector k to be the sum of separable spatial components: k_x , k_y and k_z . Hence, the longitudinal wavevector of any solution to the Helmholtz equation can subsequently be defined:

$$k_z^2 = \sqrt{k^2 - k_x^2 - k_y^2}. \quad (2.13)$$

which enables us to write the plane-wave disturbance at origin:

$$E_\omega(x, y, z) = \exp [i (k_x x + k_y y + k_z z)] \quad (2.14)$$

as the product of its transverse and longitudinal elements:

$$E_\omega(x, y, z = 0) = \exp [iz \sqrt{k^2 - k_x^2 - k_y^2}] \quad (2.15)$$

$$= \exp [i (k_x x + k_y y)] \exp [iz \sqrt{k^2 - k_x^2 - k_y^2}]. \quad (2.16)$$

From Equation 2.15 we see that:

$$E_\omega(x, y, z = 0) = \exp [i (k_x x + k_y y)] \quad (2.17)$$

which means that the evolution of the unpropagated field $E(x, y, z = 0)$ is obtained by multiplication of the initial wavefield by the free space operator $\exp [iz \sqrt{k^2 - k_x^2 - k_y^2}]$.

We can represent any E_ω as the two-dimensional Fourier integral describing the linear contribution of its plane-wave spatial components:

$$E_\omega(x, y, z = 0) = \frac{1}{2\pi} \iint E_\omega(k_x, k_y, z = 0) \exp [i(k_x x + k_y y)] dk_x dk_y \quad (2.18)$$

where each spatial component in the integral on the RHS of Equation

$$E_\omega(x, y, z = \Delta z) = \frac{1}{2\pi} \iint E_\omega(k_x, k_y, z = 0) \exp[i(k_x x + k_y y)] \\ \times \exp\left[iz\sqrt{k^2 - k_x^2 - k_y^2}\right] dk_x dk_y \quad (2.19)$$

From which we define the free-space diffraction operator, $\mathcal{D}_{\Delta z}$:

$$E_\omega(x, y, z = \Delta z) = \mathcal{D}_{\Delta z} E_\omega(x, y, z = 0) \quad (2.20)$$

$$\mathcal{D}_{\Delta z} = \mathcal{F}^{-1} \exp\left[iz\sqrt{k^2 - k_x^2 - k_y^2}\right] \mathcal{F} \quad (2.21)$$

where \mathcal{F} and \mathcal{F}^{-1} are the Fourier and inverse Fourier transforms with respect to transverse coordinates.

With this formulation, we present an algorithm for propagating any polychromatic scalar disturbance to an arbitrary parallel plane:

1. Take the angular decomposition of the polychromatic field, E into its monochromatic components E_ω via Equation 2.11.
2. Decompose each monochromatic component of the monochromatic signal into its plane-wave spatial components via Equation 2.18.
3. Multiply each of the plane wave components by the free-space Fresnel diffraction operator given in Equation 2.21.
4. Recompose each of the propagated monochromatic components as the sum of its spatial frequencies by taking the inverse Fourier transform of the R.H.S of 2.18.
5. Recompose the propagated, polychromatic electric field from the sum of its monochromatic components by taking the inverse Fourier transform of the R.H.S of 2.11.

2.1.4 Fresnel Diffraction

Collimated optical fields are considered to be paraxial when all non-negligible plane wave components make a small angle with respect to the optical axis. In this

case, the longitudinal wavevector can be expressed via the binomial approximation:

$$\sqrt{k^2 - k_x^2 - k_y^2} \approx k - \frac{k_x^2 + k_y^2}{2k} \quad (2.22)$$

allowing the free-space propagator \mathcal{D} to be re-written for the propagation of paraxial wavefields:

$$\mathcal{D}^{(F)} \equiv \exp(ik\Delta z) \mathcal{F}^{-1} \exp\left[\frac{i\Delta z (k_x^2 + k_y^2)}{2k}\right] \quad (2.23)$$

$$\begin{aligned} E_\omega(x, y, z = \Delta z) &\equiv \mathcal{D}^{(F)} E_\omega(x, y, z = 0) \\ &= \exp(ik\Delta z) \mathcal{F}^{-1} \exp\left[\frac{i\Delta z (k_x^2 + k_y^2)}{2k}\right] \mathcal{F} E_\omega(x, y, z = 0) \end{aligned} \quad (2.24)$$

where the paraxial Fresnel free-space diffraction operator is labelled $\mathcal{D}^{(F)}$

2.1.5 Sampling Requirements of the Fresnel Propagator

The issue of adequately sampling a wavefield pertains to the loss of information due to the digitisation of a continuous signal - undersampling manifests as non-physical signal artefacts due to loss of phase information of high spatial frequencies in the discretisation of fields in numerical applications, as well as physical applications (i.e. the discretisation of a physical field due to the finite resolution of an optical intensity detector). For a paraxial field, as in 2.1.4, discrete representations of the field dictate finite step sizes in the \mathcal{F} and \mathcal{F}^{-1} . Considering first the computational case³ implementation of a discrete Fourier and inverse Fourier samples on each of the transverse dimensions must sample the continuous space at an interval smaller than or equal to the Nyquist limit, N :

$$N \leq \pi k_{max}^{-1} = \pi \sigma_{max} \quad (2.25)$$

where k_{max} and σ_{max} are the extent of the wavefield in frequency and real-space. This denotes that the approximation in Equation 2.24 if the phase-gradient of ad-

³ where the available parameter space is less restrictive

jacent spatial frequencies is less than π . An expression for the satisfactory spatial step-size of the discrete field can be defined considering the maximum phase of a paraxial field propagated a distance Δz in free-space ⁴:

$$\phi_{max}^{(F)} = \frac{k}{2\Delta z\sigma_{max}}, \quad \Rightarrow \quad \frac{\partial\phi_{max}^{(F)}}{\partial k_{max}} = \pi\sigma_{max}. \quad (2.26)$$

For simplicity, consider the wavefield to be axiosymmetric so that it may be defined on the interval $[-\frac{\sigma_{max}}{2}, \frac{\sigma_{max}}{2}]$ which has a corresponding Fourier space domain $[-\frac{N}{2\sigma_{max}}, \frac{N}{2\sigma_{max}}]$ where N is the number of discrete points over which the continuous wavefield has been sampled. Defining a sampling interval $dN = \frac{\sigma_{max}}{N}$ and making use of the fact $k = \frac{2\pi}{\lambda}$, as well as Equation 2.25 and Equation 2.26 we can define the minimum sampling frequency of a paraxial field propagated through free space:

$$dN \leq \frac{\Delta z\lambda}{\sigma_{max}}. \quad (2.27)$$

In experiment, dN corresponds to the minimum spatial resolution of an optical intensity detector to avoid artefacts in representing an optical wavefield. We note that in many experimental cases this value is fixed and the issue of sampling is solved by shifting the detector downstream.

2.1.6 The Huygens-Fresnel Convolution Propagator

Equation 2.27 imposes severe restrictions on the complexity of fields that can be represented computationally as the size of any $E_\omega(x, y)$ scales with N^2 . Making use of the Fourier convolution theorem (link to appendix) by noting that the convolution of any two well behaved functions $f(x, y)$ and $g(x, y)$ can be written in terms of \mathcal{F} and \mathcal{F}^{-1} :

$$f(x, y) \otimes g(x, y) = 2\pi\mathcal{F}^{-1} \{ \mathcal{F} [f(x, y)] \mathcal{F} [g(x, y)] \} \quad (2.28)$$

allowing us to write 2.24

⁴ which occurs at the boundary of the continuous wavefield defined in real-space

$$E_\omega(x, y, z = \Delta z) = 2\pi \mathcal{F}^{-1} \left\{ \mathcal{F} \mathcal{F}^{-1} \left[\frac{1}{2\pi} \exp(ik\Delta z) \exp \left(\frac{-ik(k_x^2 + k_y^2)}{2k} \right) \right] \right. \\ \left. \times \mathcal{F} [E_\omega(x, y, z = 0)] \right\} \quad (2.29)$$

$$\equiv E_\omega(x, y, z = 0) \circledast \mathcal{D}^{(HF)}(x, y, z = \Delta z) \quad (2.30)$$

where we define $\mathcal{D}^{(HF)}$ to be the Huygens-Fresnel free-space propagation operator which formulates the propagated wavefield as the sum of electromagnetic disturbances propagated from each sampled point in the unpropagated plane as spherical waves (cite):

$$E_\omega(x, y, z = \Delta z) \approx \frac{-ik \exp(ik\Delta z)}{2\pi\Delta z} \iint E_\omega(x', y', z = 0) \\ \times \exp \left\{ \frac{ik}{2\Delta z} [(x^2 - x'^2) + (y^2 - y'^2)] \right\} dx' dy' \quad (2.31)$$

The absence of a Fourier transform on the RHS of Equation 2.31 provides a convenient method of circumventing sampling requirements in numerical propagation of free-space diffraction.

2.1.7 Fraunhofer Diffraction

Finally, we consider the limiting case where the propagation distance is far greater than the characteristic length scales of the wavefield. Factorising Equation 2.31:

$$E_\omega(x, y, z = \Delta z) \approx \frac{-ik \exp(ik\Delta z)}{2\pi\Delta z} \exp \left[\frac{ik(x^2 + y^2)}{2\Delta z} \right] \iint E_\omega(x', y', z = 0) \\ \times \exp \left[\frac{ik}{2\Delta z} [(x^2 - x'^2) + (y^2 - y'^2)] \right] dx' dy', \quad (2.32)$$

and define the Fresnel Criterion, F :

$$F \equiv \frac{\sigma^2}{\lambda\Delta z}. \quad (2.33)$$

When $F \ll 1$ the first integral in the exponent of 2.32 vanishes and we can re-write it as the Fraunhofer diffraction integral:

$$E_\omega(x, y, z = \Delta z) \approx \frac{-ik \exp(ik\Delta z)}{2\pi\Delta z} \exp\left[\frac{ik(x^2 + y^2)}{2\Delta z}\right] \times \iint E_\omega(x', y', z = \Delta z) \exp\left[\frac{-ik}{\Delta z}(xx' + yy')\right] dx' dy' \quad (2.34)$$

. Where we define any propagation distance $\Delta z : F \ll 1$ to be farfield diffraction (and its inverse to be nearfield diffraction).

2.2 X-RAY IMAGING

X-ray imaging is at the core of this. X-rays are particularly advantageous due to this, and are implemented in myriad techniques cite cite cite. In this section we describe the challenges associated with contemporary image techniques without a view of XFEL specific techniques which we reserve for this section...

2.2.1 Interaction of Light with Matter

The interaction of light with matter is at the centre of x-ray imaging. The structural information encoded in the wavefield during the coupling of the light and matter fields enables interpretation of the three-dimensional structure of the material. Here we pursue a description of the evolution of electromagnetic fields in the presence of a scattering medium, beginning with the generalised Maxwell's equations:

$$\nabla \cdot \mathbf{D}(x, y, z, t) = \rho(x, y, z, t) \quad (2.35)$$

$$\nabla \times \mathbf{H}(x, y, z, t) - \frac{\partial}{\partial t} \mathbf{D}(x, y, z, t) = \mathbf{J}(x, y, z, t) \quad (2.36)$$

where we have introduced the electric displacement vector, \mathbf{D} , and the magnetic field \mathbf{H} , charge density ρ and current density \mathbf{J} . We note that Equation 2.2 and Equation 2.3 hold as in free-space. Equation 2.35 is Gauss' law and states the proportionality of the charged enclosed within a surface and the electric displacement flux through the surface. Equation 2.36 is Maxwell's modification of Gauss' law and denotes that magnetic fields can be induced by both electric current or a changing displacement field.

In general, the displacement and induction vectors are functions of \mathbf{E} and \mathbf{B} ⁵. Restricting ourselves to the case of linear materials, let $\mathbf{D} = \epsilon \mathbf{E}$ and $\mathbf{B} = \mu \mathbf{H}$ where

5 in ferroelectric and ferromagnetic materials, \mathbf{D} and \mathbf{B} depend on the history of the material

ϵ and μ denote the electrical and magnetic permittivity of the materials. Hence, we can re-write Maxwell's equations in terms of E and B :

$$\nabla \cdot [\epsilon(x, y, z, t) E(x, y, z, t)] = \rho(x, y, z, t), \quad (2.37)$$

$$\nabla \cdot B = 0, \quad (2.38)$$

$$\nabla \times E(x, y, z, t) + \frac{\partial}{\partial t} B(x, y, z, t) = 0, \quad (2.39)$$

$$\nabla \times \left[\frac{B(x, y, z, t)}{\mu(x, y, z, t)} \right] - \frac{\partial}{\partial t} [\epsilon(x, y, z, t)] = J(x, y, z, t). \quad (2.40)$$

Making use of the vector identities Equation 6.1 and Equation 6.2 and assuming that ϵ and μ are time independent, Equation 2.39 becomes:

$$\begin{aligned} & \left[\epsilon(x, y, z) \mu(x, y, z) \frac{\partial^2}{\partial t^2} - \nabla \cdot^2 \right] E(x, y, z, t) \\ &= [\nabla \cdot \ln \mu(x, y, z)] \times [\nabla \times E(x, y, z, t)] \\ &= -\nabla \cdot [\nabla \cdot E(x, y, z, t)] - \mu(x, y, z) \frac{\partial}{\partial t} J(x, y, z, t), \end{aligned} \quad (2.41)$$

where we have used Equation 2.3 to substitute $\frac{\partial}{\partial t} B$ with $-\nabla \times E$. Which can be reduced to the d'Alembert wave equation for a generalised medium. Assuming that the scattering medium is non-magnetic: $\mu = \mu_0$ and that there is no charge or current density present: $\rho = J = 0$, the generalised form of the Helmholtz equation can be written:

$$\left[\epsilon(x, y, z) \mu_0 \frac{\partial^2}{\partial t^2} - \nabla \cdot^2 \right] E(x, y, z, t) = -\nabla \cdot [\nabla \cdot E(x, y, z, t)] \quad (2.42)$$

where the RHS of Equation 2.42 can be ignored under that condition that the material is slowly varying on lengthscales the size of a wavelength:

$$\left[\epsilon(x, y, z) \mu_0 \frac{\partial^2}{\partial t^2} - \nabla^2 \right] E(x, y, z, t) \approx 0. \quad (2.43)$$

Finally, it is responsible to consider the fact that the response of a material to incident radiation is frequency dependent. We therefore re-define Equation 2.43 using the spectral formulation (Equation 2.11

$$\int_0^\infty \{ [\nabla^2 + \epsilon_\omega(x, y, z) \mu_0 \omega^2] E_\omega(x, y, z) \} \exp(-i\omega t) = 0. \quad (2.44)$$

Clearly, the bracketed quantity in Equation 2.44 must disappear over the range of integration:

$$[\nabla^2 + \epsilon_\omega(x, y, z)\mu_0 c^2 k^2] E_\omega(x, y, z) = 0, \quad (2.45)$$

where we have made use of the fact that $\omega = ck$.

Finally, we introduce the complex refractive index of a material, n_ω :

$$n_\omega(x, y, z) = c \sqrt{\epsilon_\omega(x, y, z)\mu_0} = \sqrt{\frac{\epsilon_0 m(x, y, z)}{\epsilon_0}}, \quad (2.46)$$

yielding the inhomogeneous Helmholtz equation from Equation 2.45:

$$[\nabla^2 + k^2 n_\omega^2(x, y, z)] E_\omega(x, y, z) = 0 \quad (2.47)$$

which governs the scattering of each spectral component of an electric field in an inhomogeneous medium.

2.2.2 The Projection Approximation

The projection approximation assumes that the phase perturbations imposed by a material on the incident wavefield are sufficiently weak that the phase and amplitude disturbances at the exit-surface of the material can be expressed as the aggregate of amplitude of phase shift through the material, relative to the field in the absence of the material.

In pursuit of an approximation of the scattering of an incident plane-wave by a local distribution of *static* scatterers, consider a perturbed plane-wave solution to Equation 2.45 defined by the spatial envelope E_0 :

$$E_\omega(x, y, z) = E_0(x, y, z) \exp(-i\omega t). \quad (2.48)$$

Substituting our perturbed plane wave (Equation 2.48) into the inhomogeneous Helmholtz equation, and making use of the vector identity Equation 6.3, a solu-

tion to Equation 2.47 can be written in terms of the transverse and longitudinal components of the laplacian of the spatial envelope:

$$\left\{ 2ik \frac{\partial}{\partial z} + \nabla_{\perp}^2 + \frac{\partial^2}{\partial z^2} + k^2 [n_{\omega}(x, y, z) - 1] \right\} E_0(x, y, z) = 0, \quad (2.49)$$

where we have seperated the transverse and longitudinal components of the Laplacian, ∇^2 :

$$\nabla^2 = \frac{\partial}{\partial z} + \nabla_{\perp}^2. \quad (2.50)$$

Recognising that the second derivative with respect to z on the RHS of Equation 2.49 vanishes under the paraxial approximation, we write the inhomogeneous paraxial equation:

$$\left\{ 2ik \frac{\partial}{\partial z} + \nabla_{\perp}^2 + k^2 [n_{\omega}(x, y, z) - 1] \right\} E_0(x, y, z) = 0, \quad (2.51)$$

from which we derive the projection approximation by asserting that the implications of local scattering events are negligible and ignore the transverse laplacian in Equation 2.51:

$$\left\{ 2ik \frac{\partial}{\partial z} k^2 [n_{\omega}(x, y, z) - 1] \right\} E_0(x, y, z) = 0 \quad (2.52)$$

Equation 2.52 implies that the evolution of the electric-field envelope through a material is defined by the complex refractive index of the material:

$$\frac{\partial}{\partial z} E_0(x, y, z) \approx \frac{k}{2i} [1 - n_{\omega}^2(x, y, z)] E(x, y, z), \quad (2.53)$$

which we use to obtain the projection approximation describing the evolution of an optical field through a distance Δz of an inhomogeneous material:

$$E(x, y, z = \Delta z) = \exp \left\{ \frac{k}{2i} \int_{z=0}^{z=\Delta z} [1 - n_{\omega}^2(x, y, z)] dz \right\} E_0(x, y, z = 0) \quad (2.54)$$

Equation 2.54 is the primary solution of this subsection and will be utilised further in Chapter 3 to model the transmission of an XFEL beam through a cascaded optical system. Before moving forward, we close our discussion of the interaction of light with matter by presenting the predictions of the projection approximation.

Firstly, we decompose the complex refractive index into its real and imaginary components, ω and β_ω :

$$1 - n_\omega^2(x, y, z) = 2 [\omega(x, y, z) - i\beta_\omega(x, y, z)] \quad (2.55)$$

$$\Rightarrow E(x, y, z = \Delta z) = \exp \left\{ -ik \int_{z=0}^{z=\Delta z} [\omega(x, y, z) - i\beta_\omega(x, y, z)] dz \right\} \times E_0(x, y, z = 0). \quad (2.56)$$

the subsequent phase and intensity shifts, ϕ and I , imparted on a material of uniform thickness $\int dz = T$ are therefore:

$$\phi(x, y) = -K \int_\omega (x, y, z) dz = -k_\omega T(x, y) \quad (2.57)$$

$$I(x, y, z = \Delta z) = \left[-2k \int \beta_\omega(x, y, z) dz \right] I_0(x, y, z = 0) \quad (2.58)$$

where the scattering factors are defined:

$$\omega = \frac{r_e \lambda^2 n_e}{2\pi} \quad (2.59)$$

$$\beta_\omega = \frac{\mu_\omega}{2k}, \quad (2.60)$$

where r_e is the classical electron radius, n_e the electron density in the material and μ_ω the material's absorption coefficient, which is defined by the Beer-Lambert law:

2.2.3 Optical Coherence

Until now we have restricted ourselves to the case of idealised monochromatic or polychromatic plane-wave sources where the ensemble of electromagnetic fields, Ψ , contains only a single disturbance⁶. In reality, a thorough description of X-ray wavefields must admit that the quantum and thermal processes that govern the emission of X-ray fields are inherently probabilistic⁷ and the resulting X-ray wavefields are stochastic - we label these fields to be partially coherent and note that coherence is achieved in the limit that the density of the random fluctuations (both spatial and temporal) approaches 0, and incoherent as this density approaches infinity (is this even valid?). This discussion of coherence is pertinent to the case of XFEL wavefields generated by the quasi-spontaneous emission of thermal

⁶ Here Ψ is used to represent the ensemble set of electromagnetic fields at some point in time, where we have intentionally evoked notions similar to the continuous quantum mechanical wavefunctions describing the probabilistic set of states of the EM field.

⁷ this is not to mention the probabilistic nature of the interaction of fields with matter

distributions of relativistic electrons, where the field ensemble measured at the exit of the undulator is populated by couple radiation fields from large numbers of individual emitters with phases that fluctuate randomly in spacetime.

To describe the degree of coherence of an ensemble of electromagnetic field disturbances, we contrive the following illustrative case: Consider a set of emitters occupying a small volume and radiating quasi-monochromatic light at a mean wavelength $\bar{\lambda}$. For now, we consider the radiation of each emitter to be statistically stationary in the wide-sense: the correlation between any two temporal realisations of that field depends only on the time-lag between the realisations⁸ Suppose the emitting volume is stationary and located upstream of an thin opaque screen with a pair of pinhole perforations at locations $\mathbf{r}_{\perp,1} = (x_1, y_1)$ and $\mathbf{r}_{\perp,2} = (x_2, y_2)$ in the transverse plane. The position vector describing the relative displacement of the pinholes is therefore given: $\mathbf{r}_{\perp} = \sqrt{(x_2 - x_1)^2 + (y_2 - y_1)^2}$. We consider a single-pixel (bucket) detector located some distance Δz downstream and let $\mathbf{r}_{\parallel,1}$ and $\mathbf{r}_{\parallel,2}$ be the paths between each pinhole and the detector. The resulting disturbance measured at the detector is effectively a two-point correlation measurement of the wavefield $E_{\Phi}(x,y,z=0)$ in the plane of incidence with the screen.

The disturbance measured at the detector corresponds to the time-averaged interference pattern of disturbances $E_1(x_1, y_1, z = 0, t)$ and $E_2(x_2, y_2, z = 0, t)$ emanating from each pinhole. If the ensemble field E_{Φ} is a plane-wave the nature of the superposition of the fields is determined by the path difference $\mathbf{r}_{\parallel} = \|\mathbf{r}_{\parallel,2} - \mathbf{r}_{\parallel,1}\|$ which will be constructive or destructive when $\mathbf{r}_{\parallel} = 0$ or 1 , respectively. The phase retardations are a consequence of the finite speed of light in a vacuum, c . Knowing this, we can write the measured wavefield, $E_3(x_3, y_3, z = \Delta z, t)$:

$$E_3(x_3, y_3, z = \Delta z, t) = K_1 E(x_3, y_3, z = \Delta z, t - \frac{\mathbf{r}_{\parallel,1}}{c}) + K_2 E(x_3, y_3, z = \Delta z, t - \frac{\mathbf{r}_{\parallel,2}}{c}), \quad (2.61)$$

where K_1 and K_2 are complex numbers encapsulating information about the diffraction from the pinholes, scattering angles etc. The intensity of the recorded disturbance is given by the ensemble average of the square-modulus of Equation 2.61:

⁸ nonetheless, it is significant that we hold that this cannot always be assumed for XFEL wavefields.

$$\begin{aligned}
I(x_3, y_3, z = \Delta z) &= \left\langle \left\| K_1 E(x_3, y_3, z = \Delta z, t - \frac{r_{\parallel,1}}{c}) + K_2 E(x_3, y_3, z = \Delta z, t - \frac{r_{\parallel,2}}{c}) \right\| \right\rangle \\
&= I_1(x_1, y_1, z = 0) + I_2(x_2, y_2, z = 0) \\
&\quad + 2 \|K_1 K_2^*\| \text{Re} \langle E_1(x_1, y_1, z = 0, t - t) E^*(x_2, y_2, z = 0, t) \rangle.
\end{aligned} \tag{2.62}$$

where K_2^* denotes the complex conjugate of K_2 and the angular brackets are used to denote the ensemble average over time. In the absence of either one of the pinholes, it is evident that Equation 2.62 is reduced to the intensity pattern of the remaining pinhole. Note that we have written the time difference $t = \frac{r_{\parallel,2} - r_{\parallel,1}}{c}$. Importantly, the recorded intensity is defined by the interference term on the RHS of Equation 2.62, which is the correlation of the two-fields at the pinholes, where the phase-shift due to an optical path difference has been imposed. We define this to be the mutual coherence function, G , which is a function of the location of each pinhole in the transverse plane:

$$G(x_1, y_1, z_1; x_2, y_2, z_2; t) = \langle E_1(x_1, y_1, z_1, t - t) E^*(x_2, y_2, z_2, t) \rangle, \tag{2.63}$$

where we have now relaxed the condition that each of the pinholes exist in the same transverse plane. The mutual coherence function (Equation 2.63 predicts the visibility of fringes in a diffraction experiment (i.e. Young's Double Slit experiment) and is therefore a measure of the correlation of any two points of a field, or ensemble of, that can be directly measured. Normalising the mutual coherence function gives the complex degree of coherence, g :

$$\begin{aligned}
g(x_1, y_1, z_1; x_2, y_2, z_2; t) &= \frac{G(x_1, y_1, z_1; x_2, y_2, z_2; t)}{\sqrt{G(x_1, y_1, z_1, t = 0) G(x_2, y_2, z_2, t = 0)}} \\
&= \frac{G(x_1, y_1, z_1; x_2, y_2, z_2; t)}{\sqrt{I_1(x_1, y_1, z_1, t = 0) I_2(x_2, y_2, z_2, t = 0)}}
\end{aligned} \tag{2.64}$$

which describes the coherence of the source on the interval $g \in [0, 1]$, where $g = 0$ and $g = 1$ denote incoherence and coherence respectively.

Finally, we seek to generalise Equation 2.64 by noting that such a correlation measurement is suitable for any wavefield described in real-space and can be liberated from the need for a suitable interferometric experiment. For an statistically stationary x-ray wavefield in a volume of free-space, Ω , the complex degree of co-

herence of the field can be described for any set of coordinates $\mathbf{r}_1, \mathbf{r}_2 \in \Omega$ without the need for measurement⁹.

2.2.4 Partial Coherent Imaging

In this section we describe the role of partial coherence in defining the output of linear imaging systems, adopting the space-frequency description of partial coherence [26], [27] which is broadly applicable to a discussion of the properties of XFEL pulse ensembles in Chapter 4 and phase contrast imaging and phase retrieval mechanisms Chapter 5.

Begin with a paraxial complex scalar partially coherent wavefield, ψ_ω described by an ensemble of monochromatic components of frequency ω :

$$\psi_\omega = \left\{ E_\omega^j(x, y) c^{(j)} \right\} \quad (2.65)$$

$$\Psi = \int \psi_\omega(x, y) d\omega. \quad (2.66)$$

Ψ is the sum of each of the monochromatic components (i. e. those obtained from a polychromatic wavefield via Equation 2.11) each of which is comprised of the modal contributions of the source at frequency, ω . To maintain generality, we allow Ψ to be the ensemble of all disturbances emitted from some stochastic source, where the relative weight of the j^{th} contributing emission element to the ensemble is defined to be $c^{(j)}$. We note that the coherence of a system can be modelled by appropriate choice of modal basis and the associated weightings of each orthogonal field, for example: Gaussian Schell Model and Cosine-Gaussian Schell Model Beams [28]–[31]. For now, we do not restrict the ensemble to form an orthogonal basis, nor $c^{(j)}$ to have any dependence on spectral frequency.

With the purpose of classifying the response of an imaging system to a partially coherent field, we define the cross-spectral density of the each monochromatic ensemble, W_ω :

$$W_\omega(x_1, y_1, x_2, y_2) \equiv \langle E_\omega(x_1, y_1)^{(j)} E_\omega(x_2, y_2)^{(j)} \rangle \quad (2.67)$$

⁹ Although we are not restricted to the case of a pair of points and in some circumstances are only capable of observing wavefield coherence structures (i. e. phase-vortices) using higher order correlation functions

where angular brackets denote the ensemble average over all J realisations of ensemble. The associated spectral density is the ensemble averaged absolute square of the field associated with each angular frequency:

$$S_\omega \equiv W_\omega(x_1, x_2, y_1, y_2) = \langle \|E_\omega^{(j)}(x, y)c^{(j)}\|^2 \rangle, \quad (2.68)$$

which is the weighted average over all intensities in the set of monochromatic disturbances, giving the intensity distribution of the field to be I :

$$I(x, y) = \int S_\omega(x, y) d\omega. \quad (2.69)$$

Equation 2.67 is a descriptor of the coherence of a partially coherent field whose statistics are stationary (i.e. the correlation between each realisation of field is dependent on the time-lag between each realisation) and ergodic - which we have implicitly denoted by equating time and ensemble averages. We note that if Gaussian statistics can be assumed, all higher orders of the coherence function can be retrieved from W_ω . To explore the implications of partial coherence in an imaging context, we note that the cross-spectral density is the Fourier transform of the mutual coherence function defined in Equation 2.63.

Consider Ψ to be a partially coherent field at the entry-plane of a linear imaging system with a transmission function $\mathcal{T}_N = \mathcal{T}_1\mathcal{T}_2\mathcal{T}_3...\mathcal{T}_n$ for $n \in N$. Let \mathcal{T}_{n-1} be the object of interest and \mathcal{T}_n be the free-space propagation from the exit-surface of the object to the detector. An example of such a field is presented in [32]. Assume that the object is static, non-magnetic and elastically scattering, and that the spatial features of the object vary on length scales far greater than the radiation wavelength. The ensemble of fields at the detector is given as the coherent sum of all monochromatic components, which we define:

$$\psi_\omega(x, y, z = \Delta z) = \left\{ E_\omega^{(j)}(x, y, z = 0) c^{(j)} \mathcal{T}_N(x, y) \right\}. \quad (2.70)$$

For brevity, we have ignored the fact that the complex transmission function of the object is likely to be frequency dependent: $\mathcal{T}(x, y) = \int \mathcal{T}_\omega(x, y) d\omega$.

Immediately, such a description of the partially coherent wavefield permits the retrieval of a suite of coherence metrics (i.e. cross-spectral density, spectral density, Wigner function, vorticity) [33]. Within the context of contemporary X-ray imaging techniques however, we are instead concerned with the role of the coherence function of the wavefield in defining the detected intensity. While the challenges

of partially coherent imaging are explored further in Chapter 3, we note here that the implication of Equation 2.69 and Equation 2.70 is that the information of the coherence structure of a field is encoded in its intensity distribution. Without knowledge of the phase of the source, the coherent intensity component of any image cannot be decoupled from the coherence function of the field ensemble [34]. From an experimental viewpoint, $I(x, y)$ is subject to averaging of each of the monochromatic components of the field over the exposure time of the detector, and the spatial averaging over each detection element. The challenge of partially coherent imaging is therefore largely related to the generation of structure in the coherence function of the diffracted field that is unresolved in the digitalised image. Without omission of the pervasive role of image speckle in partially coherent imaging [35], [36] we maintain that the implications of partial coherence in an imaging context pertain not to the loss-of-information, but the construction of information on length scales unresolved by the optical system¹⁰.

The resolution of contemporary imaging techniques is limited both by the amplification of image aberrations to produce holographic speckle in coherent imaging systems [37]–[39], and loss-of-information due to feature blurring in partially coherent imaging systems [35]. In general, diffraction based imaging techniques, i.e. Coherent Diffractive Imaging (CDI) [40]–[42] and Holographic/Fresnel CDI [43]–[46], require a high degree of partial coherence, which has been extensively discussed within the context of image reconstruction and phase contrast imaging techniques [36], [47], [48].

2.3 X-RAY FREE ELECTRON LASERS

The X-ray Free Electron Laser is an optical source that lies at the nexus of laser and synchrotron technologies. Rather than laser-like production and amplification of light in an active-medium, stimulated by a master oscillator, the free electron laser operates like a vacuum-amplifier for relativistic electron bunches, which serve as the active medium. The spontaneous emission in the SASE process is encouraged by accelerating electrons through a strong magnetic field which acts as a master-signal for the amplification process. Self-amplification is achieved by the use of a long undulator to allow the selection of coherent radiation modes upon the coherent interaction of the electron beam with the radiated wavefield.

¹⁰ A particularly illuminating quote is given within the context of optical fields via [36]: "It is important to note that the 'decoherence' effect of optics is not a degradation of the inherent source coherence, but instead the creation of an entirely new component to the coherence function with a dramatically reduced coherence length."

Free electron lasers are a class of vacuum-tube devices capable of generating powerful, highly spatially coherent radiation at any wavelength [49]. while the initial demonstration of FELs operated in the infra-red regime, contemporary FEL sources provide an alternative to quantum

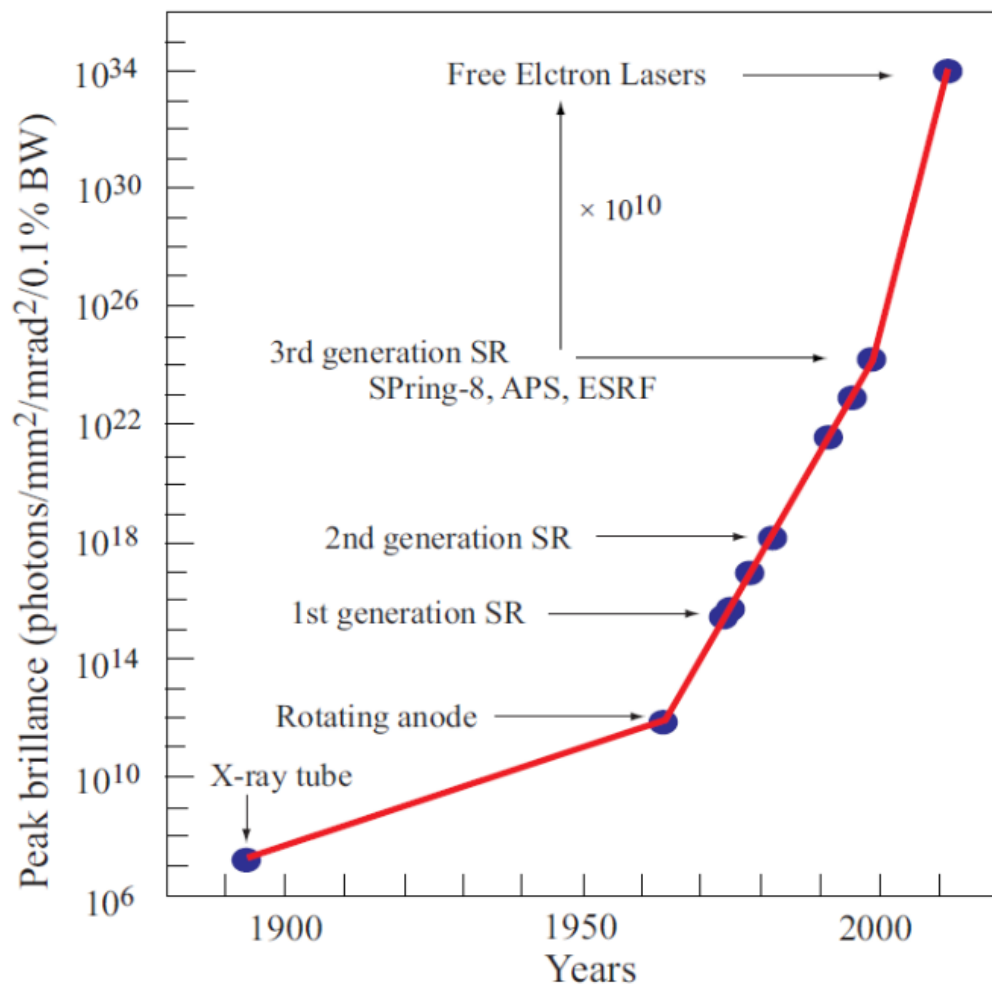


Figure 2.1

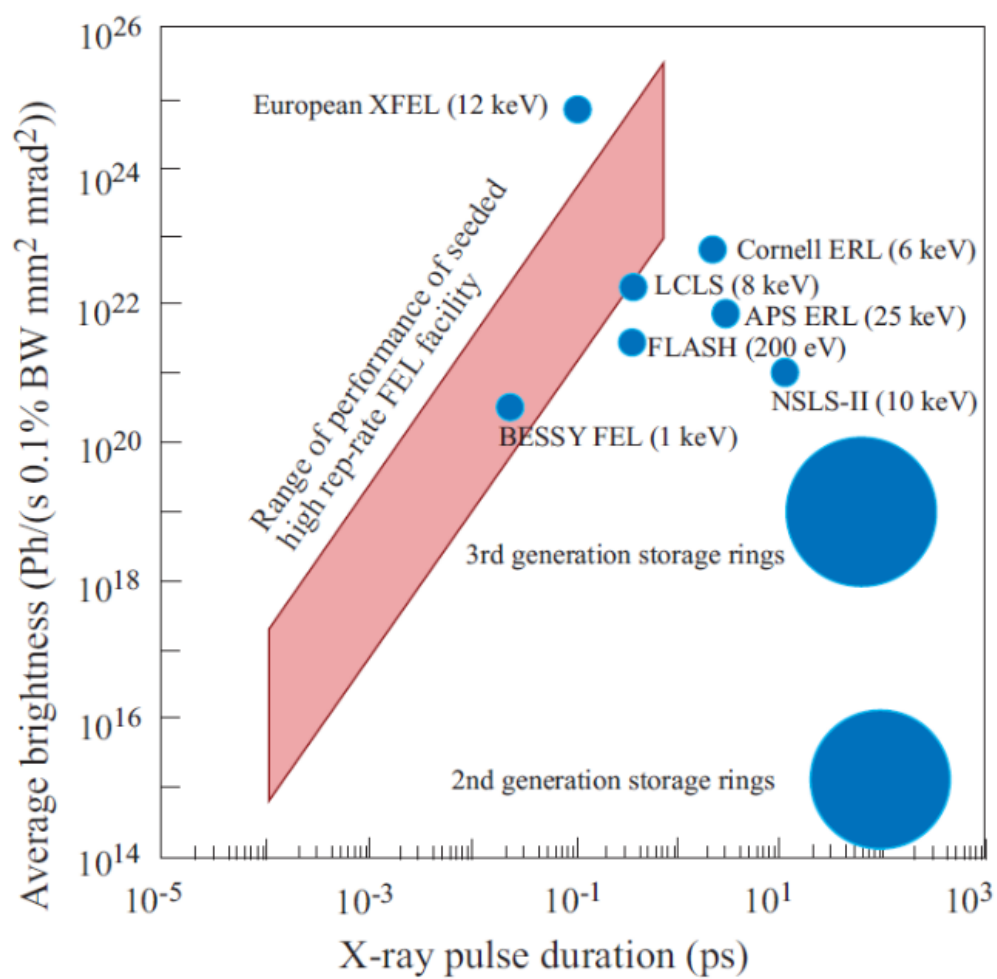


Figure 2.2

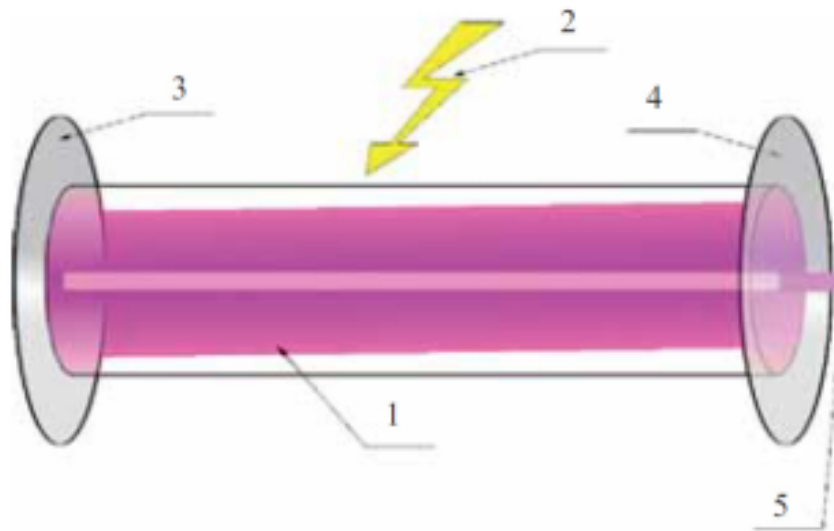


Figure 2.3

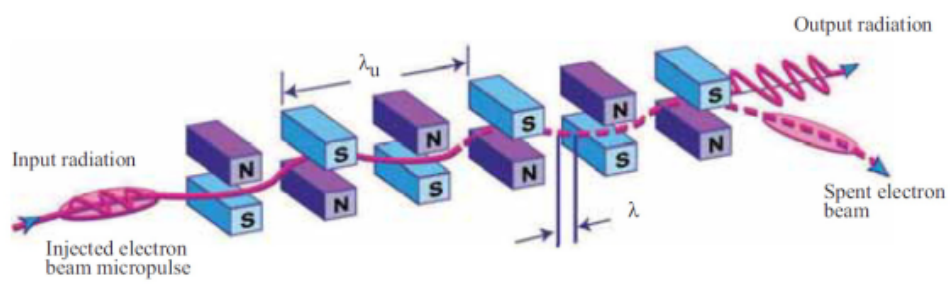


Figure 2.4

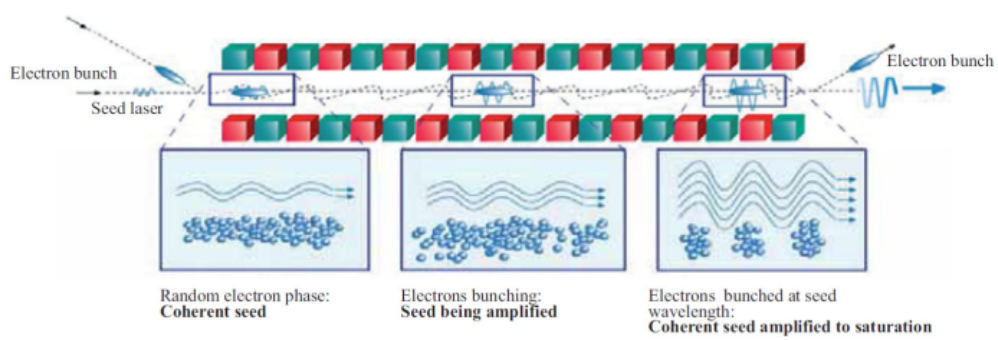


Figure 2.5

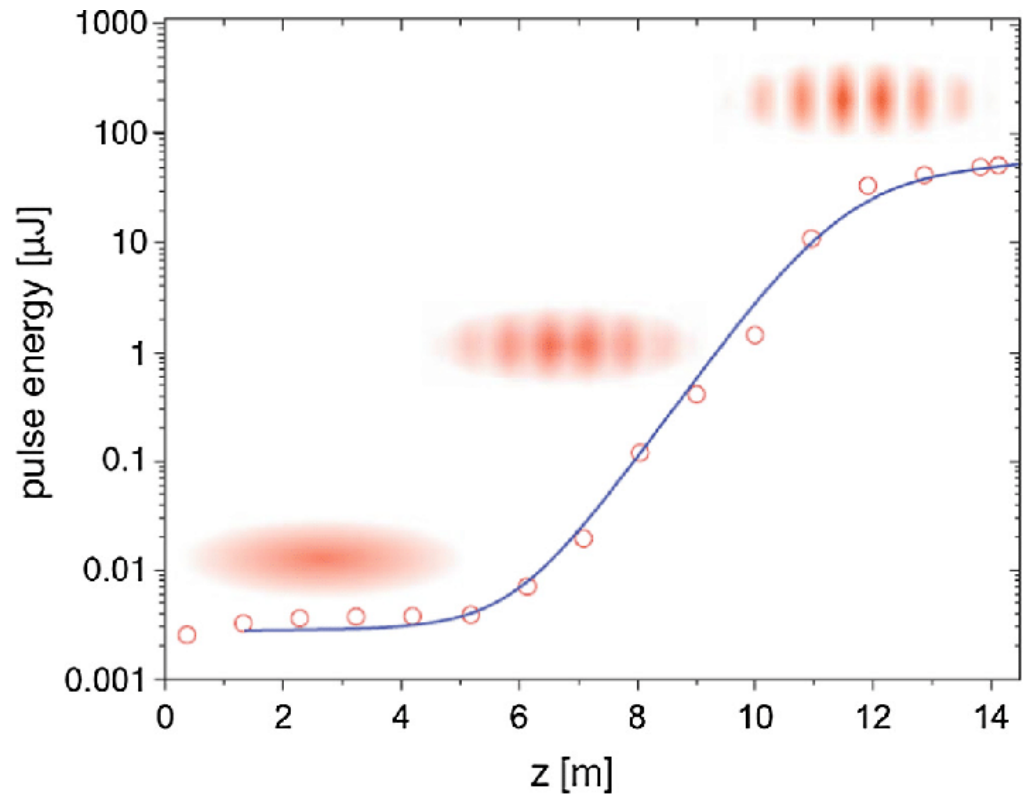


Figure 2.6

THE SPB-SFX MODEL

3.1 INTRODUCTION

The transport of X-ray radiation has been identified to be a primary factor in the disparity between theoretically achievable resolutions and current experimental benchmarks, with the improved understanding of the undulator, transport optics, focussing mirrors, front-end slits and apertures, and their role in forming the illumination-plane photon beam energy, pulse duration, beam size/shape and coherence being outlined as a primary challenge in remediating these differences [1], [50]. Understanding the intensity distribution and position in the interaction plane is essential in experimental design and plays a role in the choice of sample-to-detector distances, attenuation of photon beam power, photon energy and pulse duration [25] which are chosen to maximise the achievable resolution while satisfying oversampling requirements (Equation 2.27) and Frensel criterion (Equation 2.33). Consequently, reduced flux [51], [52] and partial coherence [53] of the illuminating wavefield are implicated in limiting the length scales accessible in imaging soft matter with hard x-rays.

The assumption of coherent illumination in CDI sample reconstructions [54] is ill-fitting in a XFEL context. Despite the development of phase-retrieval methods based on the reconstruction of the coherence function of the illuminating wavefield for 3rd generation light sources [55]–[57], the in-applicability of interferometric and ptychographic reconstruction techniques to the study of XFEL wavefields (a fact which will be discussed in more detail in Chapter 5) means that the coherence properties and subsequent response of XFEL based phase-contrast imaging systems are poorly characterised. As discussed in Section ??, the spatiotemporal coherence properties and intensity statistics of fourth generation XFEL light sources are well understood at the undulator exit in the linear-regime.

Similar sentiments cannot be shared for the non-linear (saturation) mode of operation, nor the illumination-plane beam. The requirement of grazing incidence angles for reflective hard X-ray optics truncates the beam, reducing the net

transmitted photon flux [58] and introducing intensity fringing due to diffraction from the mirror aperture that impacts the intensity profile of the illuminating beam [59], [60]. Diffraction effects alone have been attributed to 100x reductions in fluence at hard x-ray wavelengths [61]. These effects compounded by the sensitivity of short wavelength radiation to mirror surface height errors [24] and defects [62], which at-minimum (see [63]) introduce quasi-random, wavelength scale phase-perturbations on the wavefield ¹.

The development of start-to-end (S2E) simulations has been identified as a requirement for maximising the output of free electron laser facilities [25]. Here we extend on previous models of the Single Particles Clusters and Biomolecules - Serial Femtosecond Crystallography (SPB-SFX) instrument at the European XFEL [64] (add yoon citation) by improving modelling of the optical transport system, including accurate representation of residual surface height errors in the primary focussing elements, to evaluate the instrument-end beam properties for the purpose of assessing the accessible length scales in XFEL phase-contrast imaging experiments.

3.1.1 *The SPB-SFX Instrument*

SPB-SFX instrument is appended to the SASE1 beamline of the European XFEL for the structural determination of biological specimens of size $0.1\ \mu\text{m}$ to $1.0\ \mu\text{m}$ at X-ray energies between 3 keV and 16 keV [12], [65]. The optical transport system spans approximately 920 m from the undulator exit to the nominal beam focus [66].

A pair of planar horizontal offset mirrors (HOMs): HOM1 and HOM2, are located downstream of the undulator exit. HOM1 is utilised for filtering the FEL beam from high-energy bremsstrahlung and spontaneous radiation outside the design bandwidth [61]. Transport mirrors were designed to accept 4σ beam radius. Focusing of the XFEL beam is achieved independently in each of the transverse directions by a pair of Kirkpatrick-Baez mirrors [67] ². Horizontal (NHE) and vertical (NVE) elliptical mirrors are located $\approx 2.2\ \text{m}$ and $3.2\ \text{m}$ upstream of the focus. Each mirror has a 950 mm x 25 mm clear aperture. Beam conditioning is achieved by a 3.8 mm square aperture located 1.2 m upstream of the NHE. The detector modules available and associated refocussing elements are discussed elsewhere and are not relevant to a discussion of the beam focus [68]. The instrument houses two-sets of mirror configurations coated with 50 nm of reflective B_4C and Ru

¹ We chose not to discuss the implications of mirror heating in this context

² Note that in this case, we consider only the nanofocussing optical layout at the SPB-SFX instrument.

coatings for operation at photon energies of 3.0 keV - 7.5 keV and 7.5 keV - 16.0 keV respectively. A table of instrument parameters is given in Appendix 7.

3.2 METHOD

3.2.1 The Coherent Source Model

3.2.1.1 Description and Validation of the Analytical Source Model

Here we describe the construction and validation of a coherent source model that enables a study of the influence of the optical transport system in the absence of the implications of partial coherence. We note that this source provides a description of the shape and size of the SPB-SFX source using analytical data, but is a poor descriptor of the stochastic nature of XFEL pulses.

We begin with a Gaussian source defined in \mathbb{R}^3 at the undulator exit:

$$E(x, y, z = z, t) = \frac{4E_0}{\tau\sqrt{2\pi}} \frac{2\sigma_0}{2\sigma} \exp\left[\frac{(x^2 + y^2)}{2\sigma^2}\right] \exp\left[\frac{k\sqrt{(x^2 + y^2)}}{2R(z)}\right] \\ \times \exp[ikz] \exp\left[\left(\frac{-2t}{\tau}\right)^2\right] \quad (3.1)$$

where $2\sigma_0$ is the beam width at its waist, which we define to be some distance $z > 0$ upstream of the undulator exit³, 2σ is the beam radius a distance, z , downstream of the beam waist, $E_0 = E(x = 0, y = 0, z = 0, t = 0)$ and τ is the duration of the Gaussian pulse. Recognising that the radius of curvature of the beam, $R(z)$ can be written in terms of the beam divergence, θ :

$$R(z) = z \left[1 + \frac{\lambda}{\pi z \theta^2}\right]. \quad (3.2)$$

With the goal of building a Gaussian beam model with properties defined by analytical models, we aim to describe the beam in terms of measurable quantities, i.e. we aim to write Equation 3.1 in terms of 2σ and θ . Moving forward, we note that

³ where we recognise that the issue of true-source point is rarely solved for XFEL sources

$$2\sigma_0 = \frac{2\sigma}{\sqrt{1 + \frac{z\pi\theta^2}{\lambda}}} = \frac{\lambda}{\pi\theta} \quad (3.3)$$

$$\Rightarrow z = \sqrt{\frac{\pi\theta^2 2\sigma^2}{\lambda} - 1} \quad (3.4)$$

allowing the inner of the second exponent on the RHS of Equation 3.1 to be written:

$$\frac{k\sqrt{(x^2 + y^2)}}{2R(z)} = \frac{k\sqrt{x^2 + y^2}}{2} \left(\frac{\pi\theta^2 2\sigma^2}{\lambda} + \frac{4\lambda^2}{\pi^2\theta^4} - 1 \right)^{-\frac{1}{2}} = \frac{k\sqrt{x^2 + y^2}}{2\sqrt{\alpha}} \quad (3.5)$$

allowing us to re-write Equation 3.1:

$$\begin{aligned} E(x, y, z = z, t) &= \frac{E_0\lambda}{2\sigma\pi\theta} \exp \left[\frac{(x^2 + y^2)}{2\sigma^2} \right] \\ &\times \exp \left[\frac{k\sqrt{x^2 + y^2}}{2\sqrt{\alpha}} \right] \exp [ikz] \exp \left[\left(\frac{-2t}{\tau} \right)^2 \right] \end{aligned} \quad (3.6)$$

The total power of the field $E(x, y, z)$ is defined by the intensity:

$$P_0 = \frac{1}{2} \pi I_0 2\sigma_0^2 = \frac{1 \|E_0\|^2 \lambda^2}{2\pi\theta^2} \quad (3.7)$$

where the energy of the pulse is therefore:

$$U = \int_{-\tau/2}^{+\tau/2} P_0(t) dt = \frac{\tau^2 \lambda^2}{\pi\theta^2} \|E_0\|^2$$

Setting $U, \sigma, \theta = U_A, \sigma_A, \theta_A$, we define the analytical model of a pulsed Gaussian beam, E_A :

$$\begin{aligned} E_A(x, y, z = z, t) &= \sqrt{\frac{\pi^2\theta_A^2 U_A}{\tau\lambda^2}} \frac{\lambda}{2\sigma_A\pi\theta_A} \exp \left[\frac{(x^2 + y^2)}{2\sigma_A^2} \right] \\ &\times \exp \left[\frac{k\sqrt{x^2 + y^2}}{2\sqrt{\alpha_A}} \right] \exp [ikz] \exp \left[\left(\frac{-2t}{\tau} \right)^2 \right] \end{aligned} \quad (3.8)$$

Analytical fits of the properties of the SASE1 undulator at the European synchrotron are given as a function of electron beam charge and photon energy in [69] for photon energies in the range 5 keV - 40 keV. In pursuit of a geometric

model of the SASE1 source, we assess the validity of Equation 3.8 for beam properties defined by the analytical trends:

$$\sigma_A[\mu m] = a^{-1} 6 \ln \left(\frac{6000}{\lambda[nm]} \right) \quad (3.9)$$

$$\theta_A[\mu rad] = a^{-1} (13.9 - 5.17 Q[nC] \lambda[nm]^{0.85}) \quad (3.10)$$

$$U_A[mJ] = 15.4 Q[nC] \lambda[nm] \quad (3.11)$$

$$\tau_A[fs] = \frac{10^3 Q[nC]}{9.8} \quad (3.12)$$

where Q is the electron beam bunch charge, square brackets denote units and $a = \frac{1}{\sqrt{2 \ln(2)}}$ is a conversion factor between the Gaussian beam width and full-width-half-maximum (FWHM): $\sigma = \frac{FWHM}{a}$.

We define the energy of an arbitrary pulse, $E(x, y, z, t)$ to be the sum of transverse intensities intersecting some longitudinal plane, z , integrated over the duration of the pulse:

$$U(z) = \iint E(x, y, z, t) dx dy dt. \quad (3.13)$$

For calculation of the beam width and divergence, we choose to define the encircled energy of a beam in spherical coordinates:

$$E(r) = \frac{\int_0^r I(r') 2\pi r' dr'}{\int_0^\infty I(r') 2\pi r' dr'}, \quad (3.14)$$

and solve for r :

$$\operatorname{argmin}_{x \in \mathbb{R}} \left\| \frac{\int_0^r I(r') 2\pi r' dr'}{\int_0^\infty I(r') 2\pi r' dr'} - 0.5 \right\| \quad (3.15)$$

so that the beam size is defined by a radius enclosing 50% of the total beam intensity, centred at the center-of-mass of the beam, r_0 :

$$r_0 = \frac{1}{\int I_z(r) dr} \int I(r) r dr. \quad (3.16)$$

We note that this can be related to the width of a Gaussian beam which has an encircled energy, $U(r)$:

$$U(r) = 1 - \exp \left[-2 \left(\frac{r}{2\sigma} \right)^2 \right] \quad (3.17)$$

setting $E(r) = 0.5$

$$\begin{aligned} \frac{r}{2\sigma} &= \sqrt{\frac{\log(0.5)}{-2}} \approx 0.588 \\ \Rightarrow 2\sigma &= \frac{r}{\sqrt{\frac{\log(0.5)}{-2}}}. \end{aligned} \quad (3.18)$$

Finally, we define the beam divergence from its FWHM of the electric field in k -space:

$$\begin{aligned} \hat{E}(k_x, k_y) &= \frac{1}{2\pi} \iint E(x, y) \exp [-i (k_x x + k_y y)] dx dy \\ &= \mathcal{F}^{-1} [\hat{E}(k_x, k_y)] \end{aligned} \quad (3.19)$$

where we solve for $\theta = a^{-1}k_{\perp}$:

$$\operatorname{argmin}_{k_{\perp} \in \mathbb{R}} \left\| \frac{\hat{E}(0)}{\hat{E}(k_{\perp})} - \frac{1}{2} \right\|. \quad (3.20)$$

Figure 3.1 compares the modelled properties of the beam with analytical expectations and demonstrates the suitability of Equation 3.8 in representing the analytical properties of the SASE1 undulator at the European XFEL in the energy range 5 keV - 40 keV.

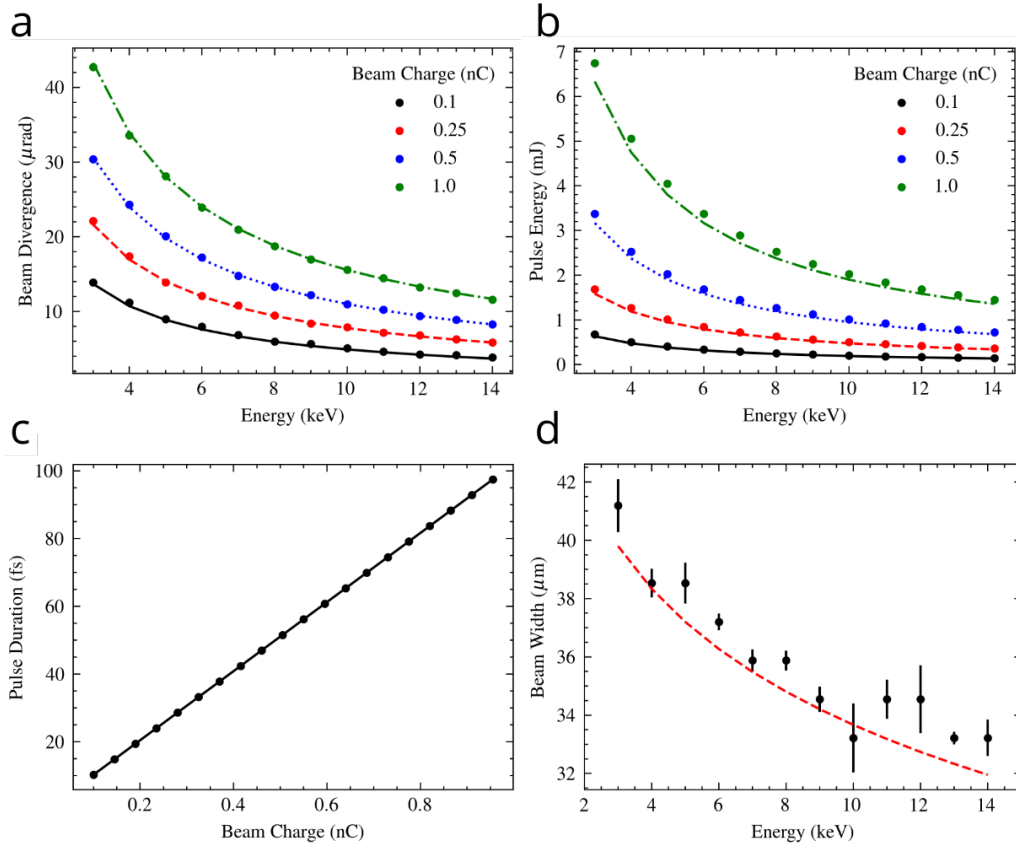


Figure 3.1: Comparison of the pulsed Gaussian beam model described in Equation 3.8 and the prescribed analytical beam a) divergence, b) pulse energy, c) pulse duration and d) 2σ pulse-width. Error bars in d) correspond to the error associated with implementation of Equation 3.15

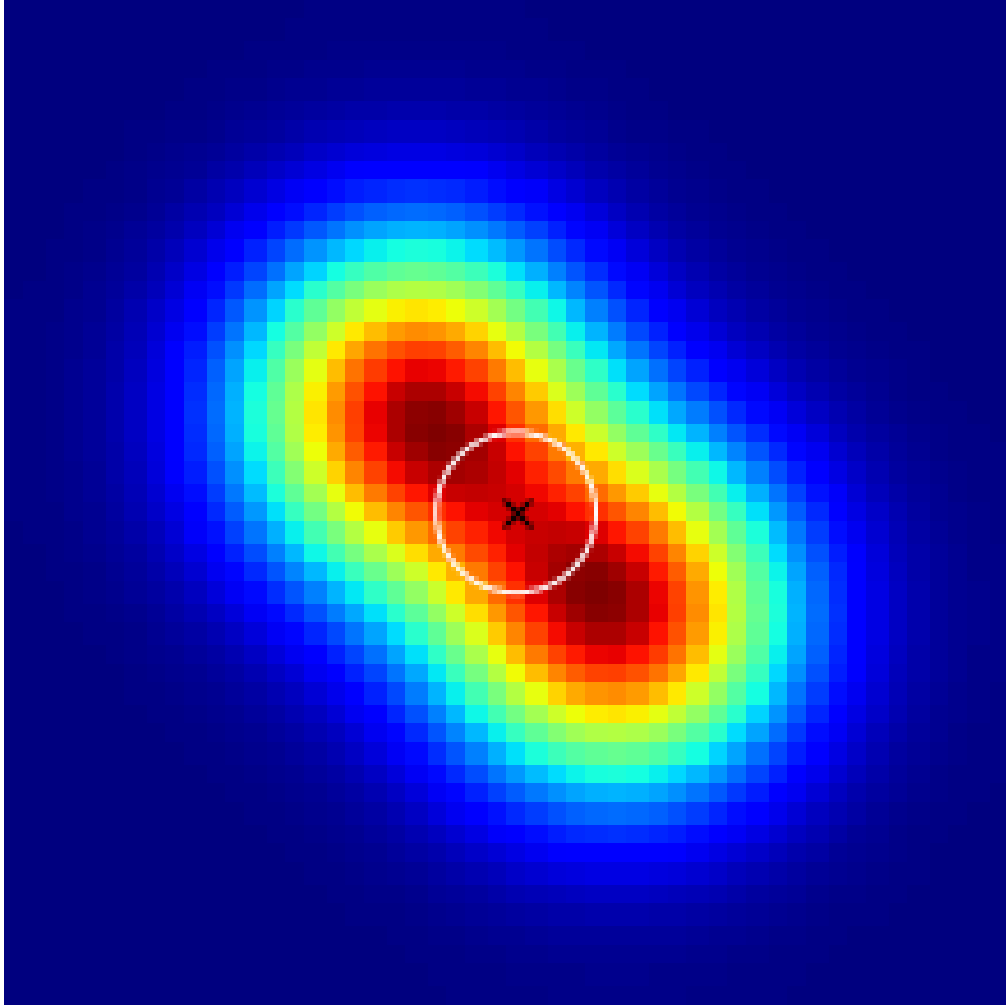


Figure 3.2

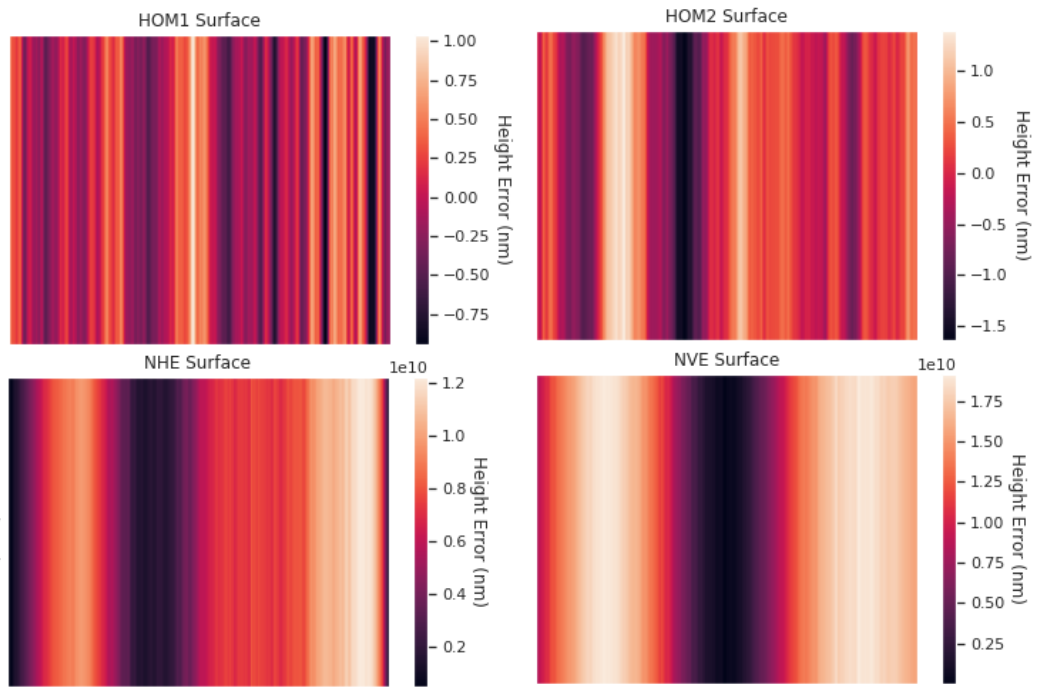


Figure 3.3

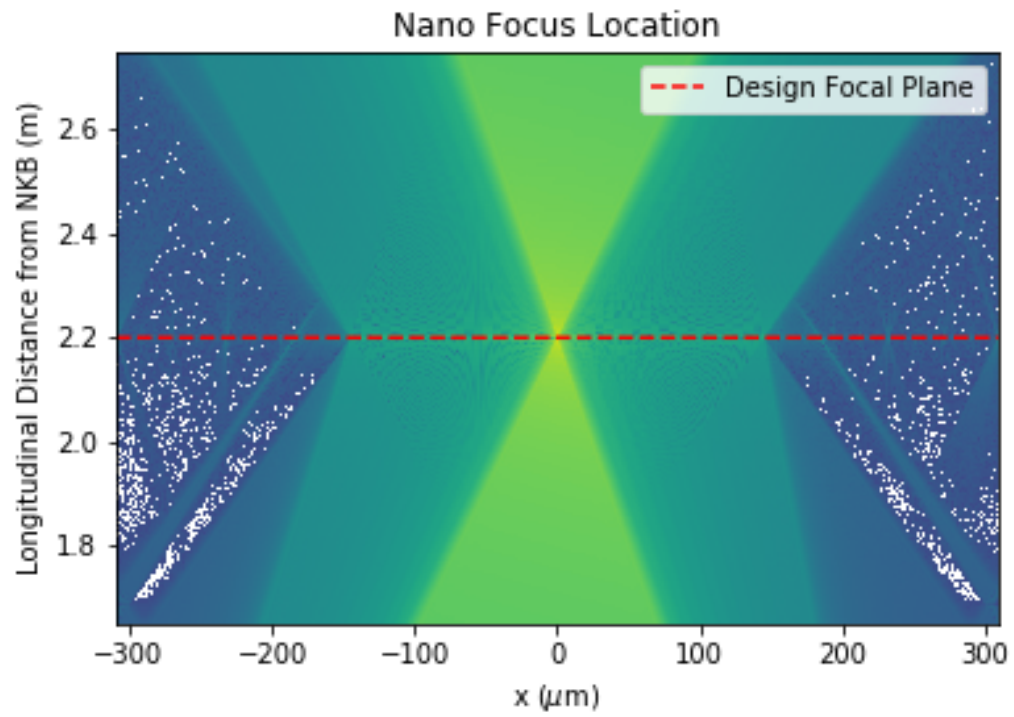


Figure 3.4

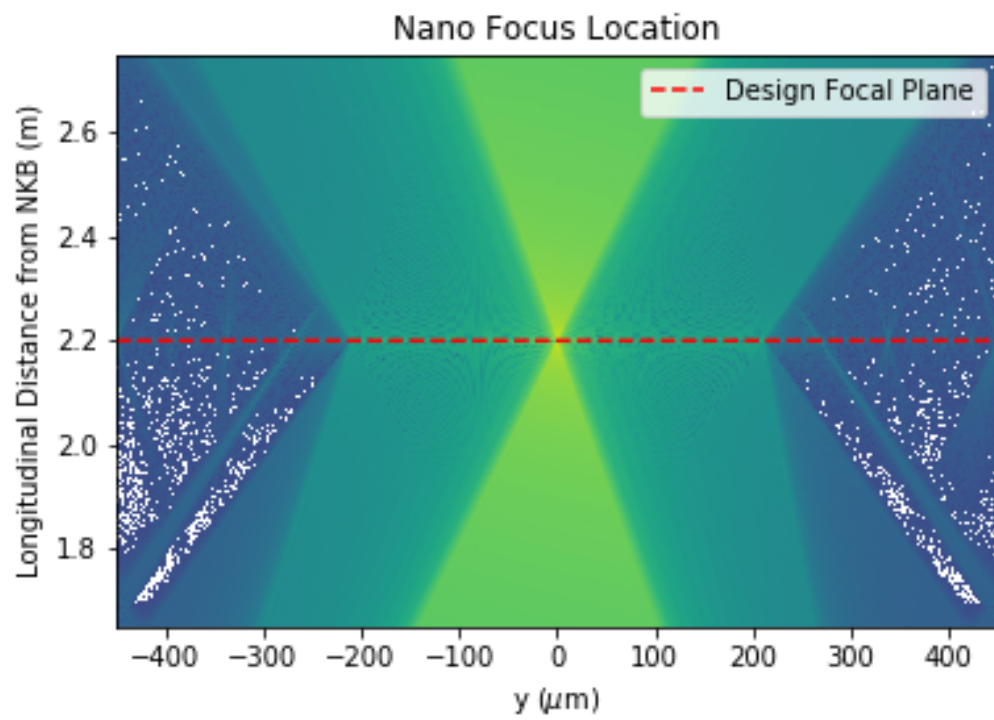


Figure 3.5

3.2.2 *The Partially Coherent Source Model*

3.2.2.1 *Description of the Partially Coherent Source*

3.2.2.2 *Comparison to Experiment*

3.3 RESULTS AND DISCUSSION

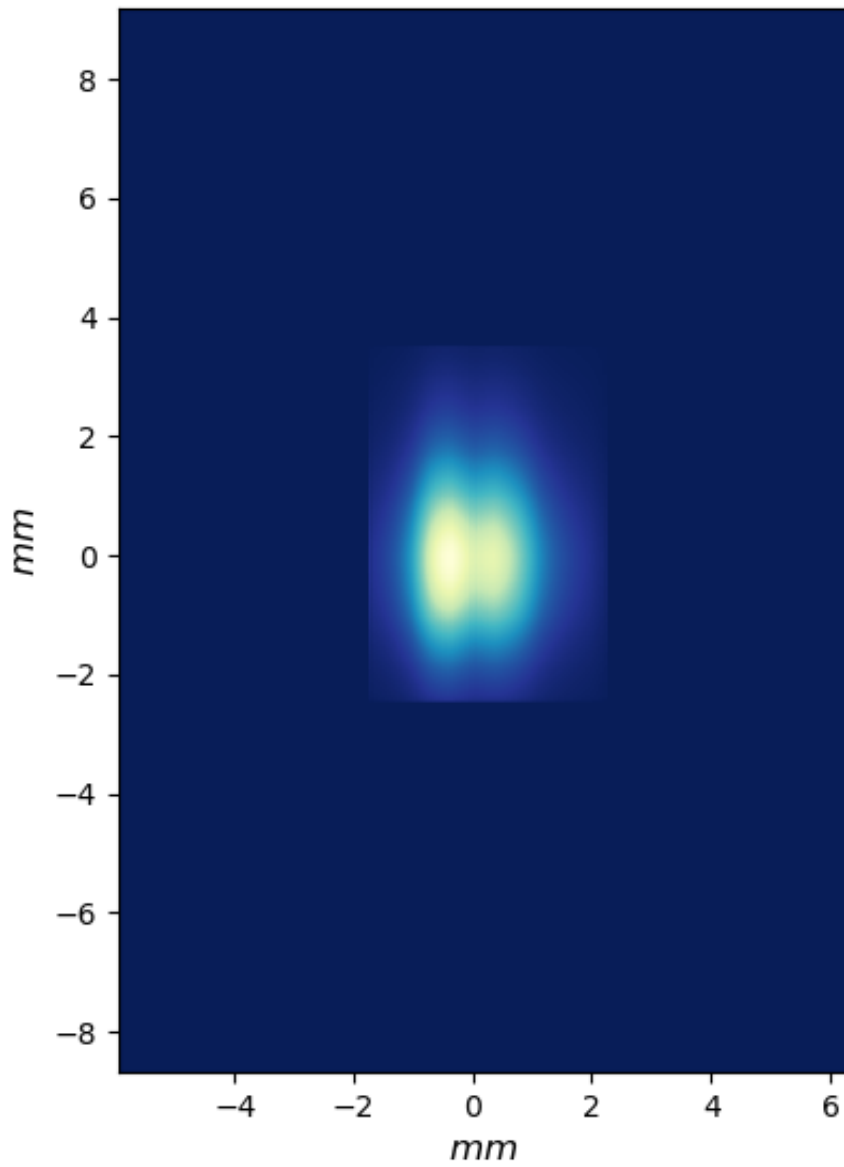


Figure 3.6

3.3.1 *Discussion*

Contemporary perspectives on CDI using XFEL beam focii fail to take into account the implications of beam transport [7], [61]

3.4 CONCLUSIONS

4

POINTING INSTABILITY AT THE SPB-SFX INSTRUMENT

4.0.1

Imaging at XFEL Facilities

4.0.2

Coherence Properties of XFEL Radiation

PHASE-RETRIEVAL METHODS FOR MHZ XFELS

5.1 INTRODUCTION

XFEL source instability is a fundamental inhibitor to the characterisation of the structure and dynamics of single proteins and macromolecule assemblies [1], [70]. While the high brilliance and ultra-fast repetition rate of XFEL sources has enabled the development and advancement of Coherent Diffractive Imaging (CDI) of non-crystalline biological samples, Serial Femtosecond Crystallography (SFX) and MegaHertz (MHz) microscopy [10], [15], [22], [71], [72] the inherent stochastic properties of the SASE x-ray generation process limit the degree to which the potential of these techniques can be realised [4], [25], [50]. While the detriment of variances in pulse fluence, spatial energy density, source coherence and beam pointing pervade XFEL literature [16], [19], [21], [73] the origin of these instabilities is poorly understood in the absence of suitable wavefront characterisation methods. Preliminary whitefield data (see below) collected using the SPB-SFX instrument at the European XFEL suggests that electron-beam parameters play a role in the pulse-pulse and train-train correlations of the source. In pursuit improved source stability, we propose a novel, single-shot MHz phase-retrieval mechanism suitable for demonstrating the role of pulse duration, bunch length, electron beam charge and energy on the coherence of the focal-plane wavefield.

5.2 VIRTUAL REFERENCE SINGLE-SHOT PHASE-RETRIEVAL

Efforts to understand and remediate phase aberrations in optical sources are pervaded by the optical-phase problem: no current detector is capable of imaging the phase and amplitude of an optical wavefront simultaneously. While phase-retrieval mechanisms for synchrotron and visible light sources are well-developed, the pulse-to-pulse instability of XFEL sources are poorly represented in classical [74] and speckle-based [75], [76] multi-shot ptychographic wavefield reconstructions. While methods for extracting independent pulses from ptychographic reconstructions of the ensemble beam phase have been reported

[77], the computational requirements of iterative phase-retrieval techniques likely prohibit the development of *online* optical phase measurement and correction infrastructures. Fine-structure variations throughout XFEL trains present a parallel challenge to dedicated single-shot grating and interference based techniques that have otherwise seen success in widefield sensing for astronomy **potier_comparing_2020** and adaptive optics [78], including but not limited to multi-slit diffraction **lupini_aberration_2010**, [79], [80], Shack-Hartmann Sensors [81], [82] and speckle-contrast analysis [83], [84], due to the imposition of stringent fabrication requirements to adequately sample phase variations at or near the focus of the XFEL beams [85].

We present a correlation-based wavefield characterisation method derivative of single-shot phase contrast imaging techniques [33] equivalent to scanning speckle-based wavefront characterisation techniques [86] as well as geometric solutions to wavefront phase using the transport of intensity equation **zuo_boundary-artifact-free_2014**, [87], [88]. Importantly, the following technique is free from the requirement of a reference image, makes no assumption on the uniformity of the incident pulse-intensities and is achievable using readily available materials.

Within the scope of optical wavefront sensing and phase retrieval, we re-imagine the sample thickness determination technique developed in [89] pulse-to-pulse perturbations in an XFEL light source. Hence, we approach a problem similar to (oriental magic mirrors, berry)

5.2.1 Absolute Mode

Consider a uniform, random phase-mask, defined by the optical transfer function $S(x,y)$:

$$S(x,y) = \exp(i\phi(x,y)) = \exp(ik\delta(x,y)T(x,y)), \quad (5.1)$$

where $\delta(x,y)$ is the real component of the refractive index and $T(x,y)$ is thickness of the mask at each point in the transverse plane.

Suppose the mask was placed in the plane immediately prior to the detector, then a phase contrast reference image, $I_R(x,y)$ would be recorded:

$$I(x,y) = \|S(x,y)\|^2, \quad (5.2)$$

where each feature in the mask is unperturbed and hence, the phase gradient at each point in the detected image is $\partial\phi_{x,y}/\partial(x,y) = \theta_{x,y} = 0$. The recorded image is labelled the virtual reference.

Note: The virtual reference satisfies the condition that:

$$S(x, y) = \mathcal{F}^{-1} \left[i\Delta z (\sqrt{k^2 - k_x^2 - k_y^2}) \right] \mathcal{F} \times S(x, y). \quad (5.3)$$

With the reference wavefield in hand, we are capable of comparing the phase perturbations present in the beam by mapping the transverse shift of phase features embedded in the beam, over the distance Δz . Consider a pulsed wavefield ψ_n with characteristic amplitude and phase distributions $A_n(x, y)$ and $\phi_n(x, y)$:

$$\phi_n(x, y) = A_n(x, y) \exp[-i\phi_n(x, y)] \quad (5.4)$$

$$I_n(x, y) = \|\mathcal{F}^{-1} \left[i\Delta z (\sqrt{k^2 - k_x^2 - k_y^2}) \right] \mathcal{F} \times \psi_n(x, y) S(x, y)\|^2. \quad (5.5)$$

, where we pursuit an absolute solution for ϕ_n .

By comparison of the unperturbed reference field with a nominal phase distribution, we can calculate the phase of the perturbed wavefield by measurement of the transverse shift of features in the array. A feature originating at some point, (x_i, y_i) in the interaction plane, that is shifted by δx and δy in each transverse dimension gives a phase gradient at the feature origin:

$$\tan(\theta_{x,y}) = \frac{\delta x / \delta y}{\Delta z}, \quad (5.6)$$

where

$$\theta_{x,y} = \frac{1}{k} \frac{\partial \phi}{\partial x / \partial y}. \quad (5.7)$$

Making use of the Fourier derivative theorem:

$$\mathcal{F} \frac{\partial \psi}{\partial r} = ik_r \mathcal{F} \psi, \quad (5.8)$$

a solution for the phase distribution of the pulse is given:

$$\phi_n(x, y) = \mathcal{F}^{-1} \left[\frac{\mathcal{F} \left(\frac{\partial \phi_x}{\partial x} + i \frac{\partial \phi_y}{\partial y} \right)}{ik_x - k_y} \right]. \quad (5.9)$$

where the origin of Fourier space is set: $\phi = 0$.

5.2.2 *Special Case*

We reserve room for the special case that the beam curvature is sufficiently large in comparison with the beam gradient that the virtual reference of the detector plane image must be scaled accordingly (see Fresnel scaling theorem).

5.2.3 *Differential Mode*

In the absence of a well-defined reference structure, the phase differential between any set of pulses can be interpreted directly from a pair of intensity images. The relative shift of phase features in the detector plane is a depiction of variations in pulse fluence and beam pointing and can consequently be seen as a natural descriptor of the coherence of a wavefield.

For a set of consecutive pulses illuminating a phase object, S , the difference in phase gradient is given by the transverse shift of features in the detector plane:

$$\tan(\Delta\theta_{x,y}) = \frac{\delta x / \delta y}{\Delta z}, \quad (5.10)$$

where

$$\Delta\theta_{x,y} = \frac{1}{k} \frac{\partial \phi}{\partial x / \partial y}. \quad (5.11)$$

APPENDIX: VECTOR IDENTITIES

$$\nabla \times [\nabla \times \mathbf{g}(x, y, z)] = \nabla [\nabla \cdot \mathbf{g}(x, y, z)] - \nabla^2 \mathbf{g}(x, y, z) \quad (6.1)$$

$$\nabla \times [f(x, y, z)\mathbf{g}(x, y, z)] = f \times [\nabla \times \mathbf{g}(x, y, z)] + [\nabla f(x, y, z)] \times \mathbf{g}(x, y, z) \quad (6.2)$$

$$\nabla^2 [f(x, y, z)\mathbf{g}(x, y, z)] = f \nabla^2 \mathbf{g} + \mathbf{g} \nabla^2 f + 2 \nabla f(x, y, z) \cdot \mathbf{g}(x, y, z) \quad (6.3)$$

APPENDIX: BEAMLINER PROPERTIES

Optical Element	Position (m)	Aperture	Operation Angles	Controlled Motion
Undulator Exit	0	-		
HOM1	246.50	x 0.5125		
		y 0.0100	Pitch 1.1 mrad - 3.6 mrad	
HOM2	246.50	x 0.5125		
		y 0.0100	Pitch 1.1 mrad - 3.6 mrad	
NKB P-SLIT	914.284	x 3.8 mm		
		y 3.8 mm	-	
		z 100 mm		
NHE	915.484	x 25 mm		x -10 mm - 5 mm
		y 950 mm	Pitch 0.5 mrad - 5.5 mrad	y - 15 mm - 15 mm
NVE	916.484	x 25 mm	Pitch - 5.5 mrad - 0.5 mrad	x -10 mm - 2 mm
		y 950 mm	Roll - 5.0 mrad - 5.0 mrad	y - 15 mm - 15 mm
			Yaw - 5.0 mrad - 5.0 mrad	
Beam Focus	918.684			

Table 7.1

BIBLIOGRAPHY

- [1] D. Oberthür, “Biological single-particle imaging using XFELs – towards the next resolution revolution,” en, *IUCr*, vol. 5, no. 6, pp. 663–666, Nov. 2018, issn: 2052-2525. doi: [10.1107/S2052252518015129](https://doi.org/10.1107/S2052252518015129). [Online]. Available: <http://scripts.iucr.org/cgi-bin/paper?S2052252518015129> (visited on 07/29/2020).
- [2] J. C. H. Spence, *High-Resolution Electron Microscopy*, Fourth Edition. Oxford, New York: Oxford University Press, Apr. 2017, isbn: 978-0-19-879583-4.
- [3] B. Henke, E. M. Gullikson, and J. C. Davis, *X-ray Interactions: Photoabsorption, Scattering, Transmission and Reflection at E = 50 - 30,000 eV, Z = 1 - 92*, ser. Atomic Data and Nuclear Data Tables 54. Academic Press, 1993.
- [4] J. C. H. Spence, U Weierstall, and H. N. Chapman, “X-ray lasers for structural and dynamic biology,” en, *Reports on Progress in Physics*, vol. 75, no. 10, p. 102 601, Oct. 2012, issn: 0034-4885, 1361-6633. doi: [10.1088/0034-4885/75/10/102601](https://doi.org/10.1088/0034-4885/75/10/102601). [Online]. Available: <https://iopscience.iop.org/article/10.1088/0034-4885/75/10/102601> (visited on 07/29/2020).
- [5] J. Drenth and J. Mesters, *Principles of protein x-ray crystallography*, en, 3rd ed. New York: Springer, 2007, isbn: 978-0-387-33334-2.
- [6] J. S. Fraser, H. v. d. Bedem, A. J. Samelson, P. T. Lang, J. M. Holton, N. Echols, and T. Alber, “Accessing protein conformational ensembles using room-temperature X-ray crystallography,” en, *Proceedings of the National Academy of Sciences*, vol. 108, no. 39, pp. 16 247–16 252, Sep. 2011, Publisher: National Academy of Sciences Section: Biological Sciences, issn: 0027-8424, 1091-6490. doi: [10.1073/pnas.1111325108](https://doi.org/10.1073/pnas.1111325108). [Online]. Available: <https://www.pnas.org/content/108/39/16247> (visited on 03/23/2021).
- [7] D. Starodub, P. Rez, G. Hembree, *et al.*, “Dose, exposure time and resolution in serial X-ray crystallography,” en, *Journal of Synchrotron Radiation*, vol. 15, no. 1, pp. 62–73, Jan. 2008, Number: 1 Publisher: International Union of Crystallography, issn: 0909-0495. doi: [10.1107/S0909049507048893](https://doi.org/10.1107/S0909049507048893). [Online]. Available: <http://scripts.iucr.org/cgi-bin/paper?pm5016> (visited on 08/12/2020).
- [8] J. C. Solem, “Imaging biological specimens with high-intensity soft x rays,” en, *Journal of the Optical Society of America B*, vol. 3, no. 11, p. 1551, Nov. 1986, issn: 0740-3224, 1520-8540. doi: [10.1364/JOSAB.3.001551](https://doi.org/10.1364/JOSAB.3.001551). [Online]. Available: <https://www.osapublishing.org/abstract.cfm?URI=josab-3-11-1551> (visited on 03/23/2021).
- [9] R. Neutze, R. Wouts, and J. Hajdu, “Potential for biomolecular imaging with femtosecond X-ray pulses,” en, vol. 406, p. 6, 2000.
- [10] H. N. Chapman, A. Barty, M. J. Bogan, *et al.*, “Femtosecond diffractive imaging with a soft-X-ray free-electron laser,” en, *Nature Physics*, vol. 2, no. 12, pp. 839–843, Dec. 2006, Number: 12 Publisher: Nature Publishing Group, issn: 1745-2481. doi: [10.1038/nphys461](https://doi.org/10.1038/nphys461). [Online]. Available: <https://www.nature.com/articles/nphys461> (visited on 03/23/2021).
- [11] S. Boutet and G. Williams, “The Coherent X-ray Imaging (CXI) instrument at the Linac Coherent Light Source (LCLS),” vol. 12, p. 035 024, Aug. 2011. doi: [10.1088/1367-2630/12/3/035024](https://doi.org/10.1088/1367-2630/12/3/035024).
- [12] A. P. Mancuso, A. Aquila, L. Batchelor, *et al.*, “The Single Particles, Clusters and Biomolecules and Serial Femtosecond Crystallography instrument of the European XFEL: Initial installation,” en, *Journal of Synchrotron Radiation*, vol. 26, no. 3, pp. 660–676, May 2019, issn: 1600-5775. doi: [10.1107/S1600577519003308](https://doi.org/10.1107/S1600577519003308). [Online]. Available: <http://scripts.iucr.org/cgi-bin/paper?S1600577519003308> (visited on 08/17/2020).
- [13] M. Altarelli, Ed., *XFEL, the European X-ray free-electron laser: technical design report*, eng. Hamburg: DESY XFEL Project Group [u.a.], 2006, OCLC: 254657183, isbn: 978-3-935702-17-1.

- [14] E. Sobolev, S. Zolotarev, K. Giewekemeyer, *et al.*, “Megahertz single-particle imaging at the European XFEL,” en, *Communications Physics*, vol. 3, no. 1, pp. 1–11, May 2020, Number: 1 Publisher: Nature Publishing Group, issn: 2399-3650. doi: [10.1038/s42005-020-0362-y](https://doi.org/10.1038/s42005-020-0362-y). [Online]. Available: <https://www.nature.com/articles/s42005-020-0362-y> (visited on 07/27/2020).
- [15] C. M. Günther, B. Pfau, R. Mitzner, *et al.*, “Sequential femtosecond X-ray imaging,” en, *Nature Photonics*, vol. 5, no. 2, pp. 99–102, Feb. 2011, issn: 1749-4885, 1749-4893. doi: [10.1038/nphoton.2010.287](https://doi.org/10.1038/nphoton.2010.287). [Online]. Available: <http://www.nature.com/articles/nphoton.2010.287> (visited on 08/20/2020).
- [16] M. F. Hantke, D. Hasse, F. R. N. C. Maia, *et al.*, “High-throughput imaging of heterogeneous cell organelles with an X-ray laser,” en, *Nature Photonics*, vol. 8, no. 12, pp. 943–949, Dec. 2014, Number: 12 Publisher: Nature Publishing Group, issn: 1749-4893. doi: [10.1038/nphoton.2014.270](https://doi.org/10.1038/nphoton.2014.270). [Online]. Available: <https://www.nature.com/articles/nphoton.2014.270> (visited on 08/24/2020).
- [17] H. P. Freund and T. M. Antonsen, *Principles of free electron lasers*, en. New York, NY: Springer Science+Business Media, 2018, ISBN: 978-3-319-75105-4.
- [18] G. Geloni, “Self-Seeded Free-Electron Lasers,” en, in *Synchrotron Light Sources and Free-Electron Lasers: Accelerator Physics, Instrumentation and Science Applications*, E. J. Jaeschke, S. Khan, J. R. Schneider, and J. B. Hastings, Eds., Cham: Springer International Publishing, 2020, pp. 191–223, ISBN: 978-3-030-23201-6. doi: [10.1007/978-3-030-23201-6_4](https://doi.org/10.1007/978-3-030-23201-6_4). [Online]. Available: https://doi.org/10.1007/978-3-030-23201-6_4 (visited on 12/15/2020).
- [19] M. Nakano, O. Miyashita, S. Jonic, A. Tokuhisa, and F. Tama, “Single-particle XFEL 3D reconstruction of ribosome-size particles based on Fourier slice matching: Requirements to reach subnanometer resolution,” en, *Journal of Synchrotron Radiation*, vol. 25, no. 4, pp. 1010–1021, Jul. 2018, issn: 1600-5775. doi: [10.1107/S1600577518005568](https://doi.org/10.1107/S1600577518005568). [Online]. Available: <http://scripts.iucr.org/cgi-bin/paper?S1600577518005568> (visited on 07/29/2020).
- [20] D. Nam, C. Kim, Y. Kim, *et al.*, “Fixed target single-shot imaging of nanostructures using thin solid membranes at SACLA,” en, *Journal of Physics B: Atomic, Molecular and Optical Physics*, vol. 49, no. 3, p. 034008, Feb. 2016, issn: 0953-4075, 1361-6455. doi: [10.1088/0953-4075/49/3/034008](https://doi.org/10.1088/0953-4075/49/3/034008). [Online]. Available: <https://iopscience.iop.org/article/10.1088/0953-4075/49/3/034008> (visited on 07/29/2020).
- [21] K. Nagaya, K. Motomura, E. Kukk, *et al.*, “Ultrafast Dynamics of a Nucleobase Analogue Illuminated by a Short Intense X-ray Free Electron Laser Pulse,” en, *Physical Review X*, vol. 6, no. 2, p. 021035, Jun. 2016, issn: 2160-3308. doi: [10.1103/PhysRevX.6.021035](https://doi.org/10.1103/PhysRevX.6.021035). [Online]. Available: <https://link.aps.org/doi/10.1103/PhysRevX.6.021035> (visited on 07/29/2020).
- [22] T. Ekeberg, M. Svenda, M. M. Seibert, *et al.*, “Single-shot diffraction data from the Mimivirus particle using an X-ray free-electron laser,” en, *Scientific Data*, vol. 3, no. 1, p. 160060, Dec. 2016, issn: 2052-4463. doi: [10.1038/sdata.2016.60](https://doi.org/10.1038/sdata.2016.60). [Online]. Available: <http://www.nature.com/articles/sdata201660> (visited on 07/29/2020).
- [23] T. Ekeberg, M. Svenda, C. Abergel, *et al.*, “Three-Dimensional Reconstruction of the Giant Mimivirus Particle with an X-Ray Free-Electron Laser,” *Physical Review Letters*, vol. 114, no. 9, p. 098102, Mar. 2015, Publisher: American Physical Society. doi: [10.1103/PhysRevLett.114.098102](https://doi.org/10.1103/PhysRevLett.114.098102). [Online]. Available: <https://link.aps.org/doi/10.1103/PhysRevLett.114.098102> (visited on 08/26/2020).
- [24] L. Samoylova, H. Sinn, F. Siewert, H. Mimura, K. Yamauchi, and T. Tschentscher, “Requirements on hard x-ray grazing incidence optics for European XFEL: Analysis and simulation of wavefront transformations,” en, R. Hudec and L. Pina, Eds., Prague, Czech Republic, May 2009, 73600E. doi: [10.1117/12.822251](https://doi.org/10.1117/12.822251). [Online]. Available: <http://proceedings.spiedigitallibrary.org/proceeding.aspx?doi=10.1117/12.822251> (visited on 07/29/2020).
- [25] A. Aquila, A. Barty, C. Bostedt, *et al.*, “The linac coherent light source single particle imaging road map,” *Structural Dynamics*, vol. 2, no. 4, p. 041701, Apr. 2015, Publisher: American Institute of Physics. doi: [10.1063/1.4918726](https://doi.org/10.1063/1.4918726). [Online]. Available: <https://aca.scitation.org/doi/full/10.1063/1.4918726> (visited on 08/12/2020).

- [26] E. Wolf, "New theory of partial coherence in the space-frequency domain Part I: Spectra and cross spectra of steady-state sources," en, *Journal of the Optical Society of America*, vol. 72, no. 3, p. 343, Mar. 1982, issn: 0030-3941. doi: [10.1364/JOSA.72.000343](https://doi.org/10.1364/JOSA.72.000343). [Online]. Available: <https://www.osapublishing.org/abstract.cfm?URI=josa-72-3-343> (visited on 08/24/2019).
- [27] L. Mandel and E. Wolf, *Optical Coherence and Quantum Optics*. Cambridge: Cambridge University Press, 1995, isbn: 978-0-521-41711-2. doi: [10.1017/CB09781139644105](https://doi.org/10.1017/CB09781139644105). [Online]. Available: <https://www.cambridge.org/core/books/optical-coherence-and-quantum-optics/F8CB94C70FA64CD3FB60890CA2048168> (visited on 04/16/2021).
- [28] A. Starikov and E. Wolf, "Coherent-mode representation of Gaussian Schell-model sources and of their radiation fields," en, *Journal of the Optical Society of America*, vol. 72, no. 7, p. 923, Jul. 1982, issn: 0030-3941. doi: [10.1364/JOSA.72.000923](https://doi.org/10.1364/JOSA.72.000923). [Online]. Available: <https://www.osapublishing.org/abstract.cfm?URI=josa-72-7-923> (visited on 02/21/2019).
- [29] A. T. Friberg and R. J. Sudol, "The Spatial Coherence Properties of Gaussian Schell-model Beams," en, *Optica Acta: International Journal of Optics*, vol. 30, no. 8, pp. 1075–1097, Aug. 1983, issn: 0030-3909. doi: [10.1080/713821334](https://doi.org/10.1080/713821334). [Online]. Available: <https://www.tandfonline.com/doi/full/10.1080/713821334> (visited on 01/17/2020).
- [30] R. Coisson and S. Marchesini, "Gauss-Schell Sources as Models for Synchrotron Radiation," en, *Journal of Synchrotron Radiation*, vol. 4, no. 5, pp. 263–266, Sep. 1997, issn: 09090495. doi: [10.1107/S0909049597008169](https://doi.org/10.1107/S0909049597008169). [Online]. Available: <http://scripts.iucr.org/cgi-bin/paper?S0909049597008169> (visited on 02/24/2019).
- [31] N. R. Van Zandt, M. W. Hyde, S. R. Bose-Pillai, D. G. Voelz, X. Xiao, and S. T. Fiorino, "Synthesizing time-evolving partially-coherent Schell-model sources," en, *Optics Communications*, vol. 387, pp. 377–384, Mar. 2017, issn: 00304018. doi: [10.1016/j.optcom.2016.10.055](https://doi.org/10.1016/j.optcom.2016.10.055). [Online]. Available: <https://linkinghub.elsevier.com/retrieve/pii/S0030401816309373> (visited on 01/22/2020).
- [32] D. Pelliccia and D. Paganin, "Coherence vortices in vortex-free partially coherent x-ray fields," English, *Physical Review A*, vol. 86, no. 1, pp. 1–4, 2012, Publisher: American Physical Society, issn: 1050-2947. doi: [10.1103/PhysRevA.86.015802](https://doi.org/10.1103/PhysRevA.86.015802). [Online]. Available: <https://research.monash.edu/en/publications/coherence-vortices-in-vortex-free-partially-coherent-x-ray-fields> (visited on 04/15/2021).
- [33] D. M. Paganin and D. Pelliccia, "Tutorials on X-ray Phase Contrast Imaging: Some Fundamentals and Some Conjectures on Future Developments," en, *arXiv:1902.00364 [physics]*, Feb. 2019, arXiv: 1902.00364. [Online]. Available: <http://arxiv.org/abs/1902.00364> (visited on 01/09/2020).
- [34] J. Clark, X. Huang, R. Harder, and I. Robinson, "High-resolution three-dimensional partially coherent diffraction imaging," en, *Nature Communications*, vol. 3, no. 1, p. 993, Jan. 2012, issn: 2041-1723. doi: [10.1038/ncomms1994](https://doi.org/10.1038/ncomms1994). [Online]. Available: <http://www.nature.com/articles/ncomms1994> (visited on 02/18/2021).
- [35] K. A. Nugent, C. Q. Tran, and A. Roberts, "Coherence transport through imperfect x-ray optical systems," EN, *Optics Express*, vol. 11, no. 19, pp. 2323–2328, Sep. 2003, Publisher: Optical Society of America, issn: 1094-4087. doi: [10.1364/OE.11.002323](https://doi.org/10.1364/OE.11.002323). [Online]. Available: <https://www.osapublishing.org/oe/abstract.cfm?uri=oe-11-19-2323> (visited on 04/16/2021).
- [36] I. Vartanyants and I. Robinson, "Origins of decoherence in coherent X-ray diffraction experiments," en, *Optics Communications*, vol. 222, no. 1-6, pp. 29–50, Jul. 2003, issn: 00304018. doi: [10.1016/S0030-4018\(03\)01558-X](https://doi.org/10.1016/S0030-4018(03)01558-X). [Online]. Available: <https://linkinghub.elsevier.com/retrieve/pii/S003040180301558X> (visited on 04/16/2021).
- [37] B. Chen, B. Abbey, R. Dilanian, et al., "Partial Coherence: A Route to Performing Faster Coherent Diffraction Imaging," en, *Journal of Physics: Conference Series*, vol. 463, p. 012033, Oct. 2013, issn: 1742-6596. doi: [10.1088/1742-6596/463/1/012033](https://doi.org/10.1088/1742-6596/463/1/012033). [Online]. Available: <http://stacks.iop.org/1742-6596/463/i=1/a=012033?key=crossref.e1cbca12d5a11cbbf0e0cfecccdfb3b8> (visited on 10/20/2019).
- [38] J. W. Goodman, "Some fundamental properties of speckle*," EN, *JOSA*, vol. 66, no. 11, pp. 1145–1150, Nov. 1976. doi: [10.1364/JOSA.66.001145](https://doi.org/10.1364/JOSA.66.001145). [Online]. Available: <https://www.osapublishing.org/josa/abstract.cfm?uri=josa-66-11-1145> (visited on 11/05/2019).

- [39] Y. Deng and D. Chu, "Coherence properties of different light sources and their effect on the image sharpness and speckle of holographic displays," *Scientific Reports*, vol. 7, Jul. 2017, issn: 2045-2322. doi: [10.1038/s41598-017-06215-x](https://doi.org/10.1038/s41598-017-06215-x). [Online]. Available: <https://www.ncbi.nlm.nih.gov/pmc/articles/PMC5517614/> (visited on 02/12/2019).
- [40] M. Krenkel, A. Markus, M. Bartels, C. Dullin, F. Alves, and T. Salditt, "Phase-contrast zoom tomography reveals precise locations of macrophages in mouse lungs," *eng, Scientific Reports*, vol. 5, p. 9973, May 2015, issn: 2045-2322. doi: [10.1038/srep09973](https://doi.org/10.1038/srep09973).
- [41] S. Zabler, P. Cloetens, J.-P. Guigay, J. Baruchel, and M. Schlenker, "Optimization of phase contrast imaging using hard x rays," *Review of Scientific Instruments*, vol. 76, no. 7, p. 073705, Jun. 2005, Publisher: American Institute of Physics, issn: 0034-6748. doi: [10.1063/1.1960797](https://doi.org/10.1063/1.1960797). [Online]. Available: <https://aip.scitation.org/doi/10.1063/1.1960797> (visited on 04/19/2021).
- [42] J. Miao, P. Charalambous, J. Kirz, and D. Sayre, "Extending the methodology of X-ray crystallography to allow imaging of micrometre-sized non-crystalline specimens," *en, Nature*, vol. 400, no. 6742, pp. 342–344, Jul. 1999, Number: 6742 Publisher: Nature Publishing Group, issn: 1476-4687. doi: [10.1038/22498](https://doi.org/10.1038/22498). [Online]. Available: <https://www.nature.com/articles/22498> (visited on 04/19/2021).
- [43] A. Snigirev, I. Snigireva, V. Kohn, S. Kuznetsov, and I. Schelokov, "On the possibilities of x-ray phase contrast microimaging by coherent high-energy synchrotron radiation," *Review of Scientific Instruments*, vol. 66, no. 12, pp. 5486–5492, Dec. 1995, Publisher: American Institute of Physics, issn: 0034-6748. doi: [10.1063/1.1146073](https://doi.org/10.1063/1.1146073). [Online]. Available: <https://aip.scitation.org/doi/10.1063/1.1146073> (visited on 04/19/2021).
- [44] P. Cloetens, W. Ludwig, J. Baruchel, D. Van Dyck, J. Van Landuyt, J. P. Guigay, and M. Schlenker, "Holotomography: Quantitative phase tomography with micrometer resolution using hard synchrotron radiation x rays," *en, Applied Physics Letters*, vol. 75, no. 19, pp. 2912–2914, Nov. 1999, issn: 0003-6951, 1077-3118. doi: [10.1063/1.125225](https://doi.org/10.1063/1.125225). [Online]. Available: <http://aip.scitation.org/doi/10.1063/1.125225> (visited on 04/19/2021).
- [45] G. J. Williams, H. M. Quiney, B. B. Dhal, C. Q. Tran, K. A. Nugent, A. G. Peele, D. Paterson, and M. D. de Jonge, "Fresnel Coherent Diffractive Imaging," *en, Physical Review Letters*, vol. 97, no. 2, p. 025506, Jul. 2006, issn: 0031-9007, 1079-7114. doi: [10.1103/PhysRevLett.97.025506](https://doi.org/10.1103/PhysRevLett.97.025506). [Online]. Available: <https://link.aps.org/doi/10.1103/PhysRevLett.97.025506> (visited on 04/19/2021).
- [46] K. A. Nugent, A. G. Peele, H. M. Quiney, and H. N. Chapman, "Diffraction with wave-front curvature: A path to unique phase recovery," *en, Acta Crystallographica Section A Foundations of Crystallography*, vol. 61, no. 3, pp. 373–381, May 2005, issn: 0108-7673. doi: [10.1107/S010876730501055X](https://doi.org/10.1107/S010876730501055X). [Online]. Available: <http://scripts.iucr.org/cgi-bin/paper?S010876730501055X> (visited on 04/19/2021).
- [47] T. Gureyev, Y. Nesterets, and F. de Hoog, "Spatial resolution, signal-to-noise and information capacity of linear imaging systems," *en, Optics Express*, vol. 24, no. 15, p. 17168, Jul. 2016, issn: 1094-4087. doi: [10.1364/OE.24.017168](https://doi.org/10.1364/OE.24.017168). [Online]. Available: <https://www.osapublishing.org/abstract.cfm?URI=oe-24-15-17168> (visited on 01/09/2020).
- [48] J. Hagemann and T. Salditt, "Coherence-resolution relationship in holographic and coherent diffractive imaging," *en, Optics Express*, vol. 26, no. 1, p. 242, Jan. 2018, issn: 1094-4087. doi: [10.1364/OE.26.000242](https://doi.org/10.1364/OE.26.000242). [Online]. Available: <https://www.osapublishing.org/abstract.cfm?URI=oe-26-1-242> (visited on 02/18/2021).
- [49] E. L. Saldin, E. A. Schneidmiller, and M. V. Yurkov, *The Physics of Free Electron Lasers*, *en, ser. Advanced Texts in Physics*. Berlin, Heidelberg: Springer Berlin Heidelberg, 2000, isbn: 978-3-642-08555-0 978-3-662-04066-9. doi: [10.1007/978-3-662-04066-9](https://doi.org/10.1007/978-3-662-04066-9). [Online]. Available: <http://link.springer.com/10.1007/978-3-662-04066-9> (visited on 08/21/2020).
- [50] Z. Sun, J. Fan, H. Li, and H. Jiang, "Current Status of Single Particle Imaging with X-ray Lasers," *en, Applied Sciences*, vol. 8, no. 1, p. 132, Jan. 2018, issn: 2076-3417. doi: [10.3390/app8010132](https://doi.org/10.3390/app8010132). [Online]. Available: <http://www.mdpi.com/2076-3417/8/1/132> (visited on 07/29/2020).

- [51] J. Hagemann and T. Salditt, "The fluence–resolution relationship in holographic and coherent diffractive imaging1," en, *undefined*, 2017. [Online]. Available: [/paper / The - fluence % E2 % 80 % 93resolution - relationship - in - holographic - Hagemann - Salditt / 26a027b3d33423006d737a766ca788b6720ed354](#) (visited on 04/19/2021).
- [52] C. Nave, "The achievable resolution for X-ray imaging of cells and other soft biological material," *IUCr*, 2020. doi: [10.1107/S2052252520002262](#).
- [53] D. M. Paganin, A. Kozlov, and T. E. Gureyev, "Spatial resolution, noise and information in the computational-imaging era," *arXiv:1909.11797 [physics]*, Sep. 2019, arXiv: 1909.11797. [Online]. Available: [http://arxiv.org/abs/1909.11797](#) (visited on 01/09/2020).
- [54] K. A. Nugent, "The measurement of phase through the propagation of intensity: An introduction," *Contemporary Physics*, vol. 52, no. 1, pp. 55–69, Jan. 2011, Publisher: Taylor & Francis _eprint: [https://doi.org/10.1080/00107514.2010.513884](#), ISSN: 0010-7514. doi: [10.1080/00107514.2010.513884](#). [Online]. Available: [https://doi.org/10.1080/00107514.2010.513884](#) (visited on 04/19/2021).
- [55] L. W. Whitehead, G. J. Williams, H. M. Quiney, D. J. Vine, R. A. Dilanian, S. Flewett, K. A. Nugent, A. G. Peele, E. Balaur, and I. McNulty, "Diffractive Imaging Using Partially Coherent X Rays," en, *Physical Review Letters*, vol. 103, no. 24, p. 243 902, Dec. 2009, ISSN: 0031-9007, 1079-7114. doi: [10.1103/PhysRevLett.103.243902](#). [Online]. Available: [https://link.aps.org/doi/10.1103/PhysRevLett.103.243902](#) (visited on 05/20/2019).
- [56] J. Hagemann and T. Salditt, "Reconstructing mode mixtures in the optical near-field," EN, *Optics Express*, vol. 25, no. 13, pp. 13 973–13 989, Jun. 2017, Publisher: Optical Society of America, ISSN: 1094-4087. doi: [10.1364/OE.25.013973](#). [Online]. Available: [https://www.osapublishing.org/oe/abstract.cfm?uri=oe-25-13-13973](#) (visited on 04/19/2021).
- [57] G. N. Tran, G. A. v. Riessen, and A. G. Peele, "Modal approach for partially coherent diffractive imaging with simultaneous sample and coherence recovery," EN, *Optics Express*, vol. 25, no. 10, pp. 10 757–10 764, May 2017, Publisher: Optical Society of America, ISSN: 1094-4087. doi: [10.1364/OE.25.010757](#). [Online]. Available: [https://www.osapublishing.org/oe/abstract.cfm?uri=oe-25-10-10757](#) (visited on 04/19/2021).
- [58] A. Aquila, R. Sobierajski, C. Ozkan, *et al.*, "Fluence thresholds for grazing incidence hard x-ray mirrors," *Applied Physics Letters*, vol. 106, no. 24, p. 241 905, Jun. 2015, Publisher: American Institute of Physics, ISSN: 0003-6951. doi: [10.1063/1.4922380](#). [Online]. Available: [https://aip.scitation.org/doi/10.1063/1.4922380](#) (visited on 04/20/2021).
- [59] J. Chalupský, P. Boháček, T. Burian, *et al.*, "Imprinting a Focused X-Ray Laser Beam to Measure Its Full Spatial Characteristics," en, *Physical Review Applied*, vol. 4, no. 1, p. 014 004, Jul. 2015, ISSN: 2331-7019. doi: [10.1103/PhysRevApplied.4.014004](#). [Online]. Available: [https://link.aps.org/doi/10.1103/PhysRevApplied.4.014004](#) (visited on 03/16/2020).
- [60] N. Gerasimova, S. Dziarzhyski, H. Weigelt, J. Chalupský, V. Hájková, L. Vyšín, and L. Juha, "In situ focus characterization by ablation technique to enable optics alignment at an XUV FEL source," *Review of Scientific Instruments*, vol. 84, no. 6, p. 065 104, Jun. 2013, Publisher: American Institute of Physics, ISSN: 0034-6748. doi: [10.1063/1.4807896](#). [Online]. Available: [https://aip.scitation.org/doi/10.1063/1.4807896](#) (visited on 04/20/2021).
- [61] K. Ayyer, G. Geloni, V. Kocharyan, E. Saldin, S. Serkez, O. Yefanov, and I. Zagorodnov, "Perspectives for imaging single protein molecules with the present design of the European XFEL," en, *Structural Dynamics*, vol. 2, no. 4, p. 041 702, Jul. 2015, ISSN: 2329-7778. doi: [10.1063/1.4919301](#). [Online]. Available: [http://aip.scitation.org/doi/10.1063/1.4919301](#) (visited on 07/29/2020).
- [62] S. Matsuyama, T. Inoue, J. Yamada, *et al.*, "Nanofocusing of X-ray free-electron laser using wavefront-corrected multilayer focusing mirrors," en, *Scientific Reports*, vol. 8, no. 1, p. 17 440, Dec. 2018, ISSN: 2045-2322. doi: [10.1038/s41598-018-35611-0](#). [Online]. Available: [http://www.nature.com/articles/s41598-018-35611-0](#) (visited on 08/12/2020).
- [63] S. Xia, D. Jukić, N. Wang, *et al.*, "Nontrivial coupling of light into a defect: The interplay of nonlinearity and topology," en, p. 27,

- [64] C. Fortmann-Grote, A. Buzmakov, Z. Jurek, *et al.*, “Start-to-end simulation of single-particle imaging using ultra-short pulses at the European X-ray Free-Electron Laser,” *en, IUCr*, vol. 4, no. 5, pp. 560–568, Sep. 2017, issn: 2052-2525. doi: [10.1107/S2052252517009496](https://doi.org/10.1107/S2052252517009496). [Online]. Available: <http://scripts.iucr.org/cgi-bin/paper?S2052252517009496> (visited on 01/09/2020).
- [65] A. P. Mancuso, A. Aquila, G. Borchers, K. Giewekemeyer, and S. I. Spb, “Scientific Instrument Single Particles, Clusters, and Biomolecules (SPB),” p. 232, 2013.
- [66] C. Fortmann-Grote, A. A. Andreev, K. Appel, *et al.*, “Simulations of ultrafast x-ray laser experiments,” *en, T. Tschentscher and L. Patthey, Eds., Prague, Czech Republic, Jun. 2017, 102370S*. doi: [10.1117/12.2270552](https://doi.org/10.1117/12.2270552). [Online]. Available: <http://proceedings.spiedigitallibrary.org/proceeding.aspx?doi=10.1117/12.2270552> (visited on 07/28/2020).
- [67] R. J. Bean, A. Aquila, L. Samoylova, and A. P. Mancuso, “Design of the mirror optical systems for coherent diffractive imaging at the SPB/SFX instrument of the European XFEL,” *en, Journal of Optics*, vol. 18, no. 7, p. 074011, Jul. 2016, issn: 2040-8978, 2040-8986. doi: [10.1088/2040-8978/18/7/074011](https://doi.org/10.1088/2040-8978/18/7/074011). [Online]. Available: <https://iopscience.iop.org/article/10.1088/2040-8978/18/7/074011> (visited on 08/17/2020).
- [68] T. Ruter, S. Hauf, M. Kuster, A. Joy, R. Ayers, M. Wing, C. H. Yoon, and A. P. Mancuso, “X-ray detector simulation pipelines for the European XFEL,” *en, in 2015 IEEE Nuclear Science Symposium and Medical Imaging Conference (NSS/MIC)*, San Diego, CA, USA: IEEE, Oct. 2015, pp. 1–4, isbn: 978-1-4673-9862-6. doi: [10.1109/NSSMIC.2015.7581998](https://doi.org/10.1109/NSSMIC.2015.7581998). [Online]. Available: <http://ieeexplore.ieee.org/document/7581998/> (visited on 07/28/2020).
- [69] H. Sinn, J. Gaudin, L. Samoylova, A. Trapp, and G. Galasso, “X-Ray Optics and Beam Transport,” *en, p. 132*, 2011.
- [70] R. Neutze, “Opportunities and challenges for time-resolved studies of protein structural dynamics at X-ray free-electron lasers,” *Philosophical Transactions of the Royal Society B: Biological Sciences*, vol. 369, no. 1647, Jul. 2014, issn: 0962-8436. doi: [10.1098/rstb.2013.0318](https://doi.org/10.1098/rstb.2013.0318). [Online]. Available: <https://www.ncbi.nlm.nih.gov/pmc/articles/PMC4052859/> (visited on 11/26/2020).
- [71] P. Vagovič, T. Sato, L. Mikeš, *et al.*, “Megahertz x-ray microscopy at x-ray free-electron laser and synchrotron sources,” *EN, Optica*, vol. 6, no. 9, pp. 1106–1109, Sep. 2019, Publisher: Optical Society of America, issn: 2334-2536. doi: [10.1364/OPTICA.6.001106](https://doi.org/10.1364/OPTICA.6.001106). [Online]. Available: <https://www.osapublishing.org/optica/abstract.cfm?uri=optica-6-9-1106> (visited on 11/26/2020).
- [72] S. Pandey, R. Bean, T. Sato, *et al.*, “Time-resolved serial femtosecond crystallography at the European XFEL,” *en, Nature Methods*, vol. 17, no. 1, pp. 73–78, Jan. 2020, issn: 1548-7091, 1548-7105. doi: [10.1038/s41592-019-0628-z](https://doi.org/10.1038/s41592-019-0628-z). [Online]. Available: <http://www.nature.com/articles/s41592-019-0628-z> (visited on 01/09/2020).
- [73] N. D. Loh, M. J. Bogan, V. Elser, *et al.*, “Cryptotomography: Reconstructing 3D Fourier Intensities from Randomly Oriented Single-Shot Diffraction Patterns,” *Physical Review Letters*, vol. 104, no. 22, p. 225 501, Jun. 2010, Publisher: American Physical Society. doi: [10.1103/PhysRevLett.104.225501](https://doi.org/10.1103/PhysRevLett.104.225501). [Online]. Available: <https://link.aps.org/doi/10.1103/PhysRevLett.104.225501> (visited on 08/24/2020).
- [74] S. Sala, B. Daurer, M. Hantke, T. Ekeberg, N. Loh, F. Maia, and P. Thibault, “Ptychographic imaging for the characterization of X-ray free-electron laser beams,” *en, Journal of Physics: Conference Series*, vol. 849, p. 012 032, Jun. 2017, issn: 1742-6588, 1742-6596. doi: [10.1088/1742-6596/849/1/012032](https://doi.org/10.1088/1742-6596/849/1/012032). [Online]. Available: <https://iopscience.iop.org/article/10.1088/1742-6596/849/1/012032> (visited on 07/29/2020).
- [75] A. J. Morgan, K. T. Murray, M. Prasciolu, *et al.*, “Ptychographic X-ray speckle tracking with multi-layer Laue lens systems,” *en, Journal of Applied Crystallography*, vol. 53, no. 4, pp. 927–936, Aug. 2020, issn: 1600-5767. doi: [10.1107/S1600576720006925](https://doi.org/10.1107/S1600576720006925). [Online]. Available: <http://scripts.iucr.org/cgi-bin/paper?S1600576720006925> (visited on 09/10/2020).

- [76] S. Berujon, E. Ziegler, and P. Cloetens, "X-ray pulse wavefront metrology using speckle tracking," en, *Journal of Synchrotron Radiation*, vol. 22, no. 4, pp. 886–894, Jul. 2015, issn: 1600-5775. doi: [10.1107/S1600577515005433](https://doi.org/10.1107/S1600577515005433). [Online]. Available: <http://scripts.iucr.org/cgi-bin/paper?S1600577515005433> (visited on 08/04/2020).
- [77] S. Sala, B. J. Daurer, M. Odstrcil, F. Capotondi, E. Pedersoli, M. F. Hantke, M. Manfredda, N. D. Loh, P. Thibault, and F. R. N. C. Maia, "Pulse-to-pulse wavefront sensing at free-electron lasers using ptychography," en, *arXiv:1901.08970 [physics]*, Nov. 2019, arXiv: 1901.08970. [Online]. Available: <http://arxiv.org/abs/1901.08970> (visited on 09/02/2020).
- [78] E. Abraham, H. Cahyadi, M. Brossard, J. Degert, E. Freysz, and T. Yasui, "Development of a wavefront sensor for terahertz pulses," *Optics Express*, vol. 24, no. 5, pp. 5203–5211, 2016, Publisher: Optical Society of America - OSA Publishing. doi: [10.1364/OE.24.005203](https://doi.org/10.1364/OE.24.005203). [Online]. Available: <https://hal.archives-ouvertes.fr/hal-01297343> (visited on 11/15/2020).
- [79] D. Paterson, B. Allman, P. McMahon, *et al.*, "Spatial coherence measurement of X-ray undulator radiation," en, *Optics Communications*, vol. 195, no. 1-4, pp. 79–84, Aug. 2001, issn: 00304018. doi: [10.1016/S0030-4018\(01\)01276-7](https://doi.org/10.1016/S0030-4018(01)01276-7). [Online]. Available: <https://linkinghub.elsevier.com/retrieve/pii/S0030401801012767> (visited on 05/20/2019).
- [80] P. Wachulak, A. Sarzyński, A. Bartnik, T. Fok, Węgrzynski, J. Kostecki, and H. Fiedorowicz, "Spatial coherence measurements of the EUV emission from laser-plasma source based on xenon/helium gas puff target," en, *Applied Physics B*, vol. 123, no. 8, Aug. 2017, issn: 0946-2171, 1432-0649. doi: [10.1007/s00340-017-6795-7](https://doi.org/10.1007/s00340-017-6795-7). [Online]. Available: <http://link.springer.com/10.1007/s00340-017-6795-7> (visited on 02/18/2019).
- [81] L. Freisem, G. S. M. Jansen, D. Rudolf, K. S. E. Eikema, and S. Witte, "Spectrally resolved single-shot wavefront sensing of broadband high-harmonic sources," *Optics Express*, vol. 26, no. 6, p. 6860, Mar. 2018, arXiv: 1712.04234, issn: 1094-4087. doi: [10.1364/OE.26.006860](https://doi.org/10.1364/OE.26.006860). [Online]. Available: <http://arxiv.org/abs/1712.04234> (visited on 06/01/2020).
- [82] B. Keitel, E. Plönjes, S. Kreis, M. Kuhlmann, K. Tiedtke, T. Mey, B. Schäfer, and K. Mann, "Hartmann wavefront sensors and their application at FLASH," en, *Journal of Synchrotron Radiation*, vol. 23, no. 1, pp. 43–49, Jan. 2016, issn: 1600-5775. doi: [10.1107/S1600577515020354](https://doi.org/10.1107/S1600577515020354). [Online]. Available: <http://scripts.iucr.org/cgi-bin/paper?S1600577515020354> (visited on 03/16/2020).
- [83] K. Yun, S. Kim, D. Kim, *et al.*, "Coherence and pulse duration characterization of the PAL-XFEL in the hard X-ray regime," *Scientific Reports*, vol. 9, Mar. 2019, issn: 2045-2322. doi: [10.1038/s41598-019-39765-3](https://doi.org/10.1038/s41598-019-39765-3). [Online]. Available: <https://www.ncbi.nlm.nih.gov/pmc/articles/PMC6397240/> (visited on 01/21/2020).
- [84] I. Zanette, T. Zhou, A. Burvall, U. Lundström, D. Larsson, M. Zdora, P. Thibault, F. Pfeiffer, and H. Hertz, "Speckle-Based X-Ray Phase-Contrast and Dark-Field Imaging with a Laboratory Source," *Physical Review Letters*, vol. 112, no. 25, p. 253903, Jun. 2014, Publisher: American Physical Society. doi: [10.1103/PhysRevLett.112.253903](https://doi.org/10.1103/PhysRevLett.112.253903). [Online]. Available: <https://link.aps.org/doi/10.1103/PhysRevLett.112.253903> (visited on 08/04/2020).
- [85] F. Soldevila, V. Durán, P. Clemente, J. Lancis, and E. Tajahuerce, "Phase imaging by spatial wavefront sampling," en, *Optica*, vol. 5, no. 2, p. 164, Feb. 2018, issn: 2334-2536. doi: [10.1364/OPTICA.5.000164](https://doi.org/10.1364/OPTICA.5.000164). [Online]. Available: <https://www.osapublishing.org/abstract.cfm?URI=optica-5-2-164> (visited on 06/01/2020).
- [86] M.-C. Zdora, "State of the Art of X-ray Speckle-Based Phase-Contrast and Dark-Field Imaging," *Journal of Imaging*, vol. 4, p. 60, Apr. 2018. doi: [10.3390/jimaging4050060](https://doi.org/10.3390/jimaging4050060).
- [87] T. E. Gureyev, A. Roberts, and K. A. Nugent, "Phase retrieval with the transport-of-intensity equation: Matrix solution with use of Zernike polynomials," en, *Journal of the Optical Society of America A*, vol. 12, no. 9, p. 1932, Sep. 1995, issn: 1084-7529, 1520-8532. doi: [10.1364/JOSAA.12.001932](https://doi.org/10.1364/JOSAA.12.001932). [Online]. Available: <https://www.osapublishing.org/abstract.cfm?URI=josaa-12-9-1932> (visited on 09/16/2020).
- [88] K. M. Pavlov, Heyang, Li, D. M. Paganin, S. Berujon, H. Rougé-Labriet, and E. Brun, "Single-shot x-ray speckle-based imaging of a single-material object," en, *arXiv:1908.00411 [physics]*, Jul. 2019, arXiv: 1908.00411. [Online]. Available: <http://arxiv.org/abs/1908.00411> (visited on 01/09/2020).

- [89] K. S. Morgan, D. M. Paganin, and K. K. W. Siu, "Quantitative single-exposure x-ray phase contrast imaging using a single attenuation grid," EN, *Optics Express*, vol. 19, no. 20, pp. 19 781–19 789, Sep. 2011, Publisher: Optical Society of America, issn: 1094-4087. doi: [10.1364/OE.19.019781](https://doi.org/10.1364/OE.19.019781). [Online]. Available: <https://www.osapublishing.org/oe/abstract.cfm?uri=oe-19-20-19781> (visited on 11/13/2020).